7 Oxford-RAL Aerosol and Cloud (ORAC): aerosol retrievals from satellite radiometers

Gareth E. Thomas, Elisa Carboni, Andrew M. Sayer, Caroline A. Poulsen, Richard Siddans, Roy G. Grainger

1. Introduction

This chapter describes an optimal estimation retrieval scheme for the derivation of the properties of atmospheric aerosol from top-of-atmosphere (TOA) radiances measured by satellite-borne visible-IR radiometers. The algorithm makes up part of the Oxford-RAL Aerosol and Cloud (ORAC) retrieval scheme (the other part of the algorithm performs cloud retrievals and is described in detail elsewhere [by Watts *et al.*] [37]).

The following sections will describe three separate versions of the ORAC algorithm. The first is the original ORAC aerosol retrieval algorithm, which has already been applied in producing global aerosol datasets from ATSR-2, AATSR and SEVIRI measurements (brief descriptions of these instruments are given in Section 2), through the GRAPE and GlobAEROSOL projects. This algorithm makes use of visible and near-infrared channels and assumes the Earth's surface acts as a Lambertian reflector.

The second version improves on the original Lambertian ORAC, by implementing a new forward model which uses a bi-directional reflectance distribution function (BRDF) to describe the surface reflectance. This forward model is more accurate and also allows the use of multiple views of the same scene (as are produced by the (A)ATSR instruments) to be incorporated into the retrieval.

Thirdly, a version of ORAC is described which makes use of thermal infrared channels, which greatly improve the detection of lofted dust above desert surfaces.

Finally, example results produced with all three versions of the ORAC algorithm will be presented and compared, both with each other, ground-based measurements and other satellite aerosol products.

2. Instrument descriptions

2.1 The ATSR-2 and AATSR instruments

The second and third generation Along-Track Scanning Radiometers (ATSR-2 and Advanced ATSR) were launched on the ESA polar orbit satellites ERS-2 and ENVISAT in 1995 and 2002, respectively. As the instruments are essentially the same in their operation, with the only major difference being the bandwidth available for data transfer, they can be described together.

The primary design goal of the ATSR instruments is the measurement of sea-surface temperature, with a secondary objective of ATSR-2 and AATSR being the determination

of land surface and vegetation properties. ORAC makes use of the atmospheric component of the ATSR signal, which is considered contamination in its primary and secondary roles.

Both ATSR-2 and AATSR have seven spectral channels centered at 0.55, 0.67, 0.87, 1.6, 3.7, 10.7 and 12 μm. The instruments use a dual-view system, with a continuously rotating scan mirror directing radiation from two apertures and two onboard blackbody calibration targets onto the radiometer. One viewing aperture produces a scan centered on the nadir direction, while the other views the surface approximately 900 km ahead of the satellite (at a viewing angle of 55° from the nadir). This continuous scanning pattern produces a nadir resolution of approximately 1×1 km with a swath width of 512 pixels. The dual-view system is one of the great strengths of the ATSR instruments, as it allows the atmospheric and surface contributions to the TOA radiance to be more effectively decoupled than is possible with a single view. This offers much improved accuracy in both derived surface and atmospheric parameters. In addition, the instruments are designed to be self-calibrating, with two integrated, thermally controlled blackbody targets for calibration of the thermal channels, as well as an opal visible calibration target (illuminated by sunlight) for the visible/near-IR channels.

Due to bandwidth limitations on the ERS-2 satellite, ATSR-2 is usually run in a 'narrow swath' mode over the oceans, which produces a swath of only 256 pixels in some of the visible channels (with the 0.55 μm channel being the most commonly effected, followed by 0.67 μm). In addition, although ATSR-2 is still operational, the ERS-2 satellite developed a pointing problem in October 2001, which means that post-2001 data from the instrument has to have a geo-location correction applied before it can be used. Additionally, in June 2003, the data tape recorder on ERS-2 failed, with the result that ATSR-2 data from this date is only available while the satellite is within range of a data downlink ground station. ATSR-2 ceased operating in February 2008, when the scan mirror mechanism failed.

ERS-2 and ENVISAT are in similar polar orbits with periods of approximately 100 minutes. Both ATSR-2 and AATSR nominally provide global coverage every 6 days.

2.2 The SEVIRI instrument

The Spinning Enhanced Visible and InfraRed Imager (SEVIRI) is a line-scanning radiometer and has been the primary instrument onboard the European geostationary[1] meteorological satellites since Meteosat-8 began operation. The satellite was launched in 2003 and the first data were available in early 2004. In April 2007 Meteosat-9 took over as the primary operational satellite.

SEVIRI provides data in four visible and near-infrared channels and eight infrared channels with a resolution of 3 km at the sub-satellite point. The channels used in the analysis presented here are the 0.67, 0.87 and 1.6 μm in the visible and near-infrared, with the 10.8 and 12.0 μm being used from the thermal infrared. A key feature of SEVIRI is its ability to continuously image the Earth every 15 minutes. This allows the tracking of fast-moving aerosol events, such as dust storms, which offers a great advantage over polar orbiting instruments. Also, although SEVIRI lacks the dual-view capability of the ATSR instruments, in conditions of relatively stable aerosol loading, the change in solar elevation

[1] The Meteosat sub-satellite point is at 0° longitude, just to the east of the African coastline.

throughout the day can be utilized to provide repeated views under different angles of illumination. The difference in the surface BRDF and aerosol scattering phase function can then be used to decouple the aerosol and surface signals in a way analogous to the dual-view system. The main disadvantage of this instrument is the susceptibility of the larger field-of-view to contamination by cloud.

3. The ORAC forward model

The core of the ORAC retrieval algorithm is the forward model, which uses radiative transfer code to predict the radiance observed at the satellite as a function of aerosol properties, using assumptions about the atmospheric state and the reflectance of the Earth's surface. For the sake of numerical efficiency, ORAC makes use of two forward models: firstly a full radiative transfer model (referred to here simply as the forward model, FM), which attempts to accurately account for all relevant physical processes effecting the measurement, is run 'off-line' to produce look-up tables of total atmospheric reflectance and transmission for the plausible range of viewing geometries and aerosol states. These look-up tables are then used to produce TOA radiances during a retrieval run using a simple arithmetic expression, known as the fast forward model (Fast-FM). This section details the aerosol FM used with ORAC, which is the same for both the Lambertian and BRDF surface reflectance versions of the retrieval scheme, as well as describing the extensions needed to incorporate thermal infrared channels into the retrieval scheme.

The FM can itself be thought of as consisting of three separate elements:

1. A model of aerosol scattering and absorption.
2. A model of atmospheric gas absorption.
3. Radiative transfer code to produce TOA radiance based on the output of the first two models, Rayleigh scattering and viewing geometry.

3.1 Aerosol scattering and absorption

In a given location, atmospheric aerosols are characterized by their morphology, concentration, size distribution, chemical composition (which determines their complex refractive index), and their vertical profile. With knowledge of these properties, the required radiative characteristics may be approximated by assuming the particles are spherical and applying Mie theory [20].

The aerosol optical depth, τ, is the primary quantity obtained from ORAC. It is defined as:

$$\tau(\lambda) = \int_0^\infty \beta_e(z,\lambda)\mathrm{d}z = \int_0^\infty (\beta_s(z,\lambda) + \beta_{-\alpha}(z,\lambda))\mathrm{d}z \quad (1)$$

The total extinction coefficient, β_e, is defined as the sum of the extinction due to absorption, β_a, and scattering, β_s. The vertical profile of β_a and β_s along with the scattering phase function, $P(\theta)$, which determines the angular distribution of the scattered radiation, and the degree of polarization as a function of scattering angle, fully describe the aerosol radiative characteristics. Other convenient ways of defining aerosol optical properties are the single

scattering albedo, ω_o, which is the ratio of β_s to β_e, and the asymmetry parameter, g, which is the integral of $P(\theta)$ over all possible scattering angles ($0 \leq \theta \leq 180°$), weighted by $\cos\theta$ (i.e. it is the first moment of the phase function). For a given aerosol model (shape, size, and refractive index), β_e is proportional to the aerosol concentration while $P(\theta)$ is not.

Mie theory shows that the extinction coefficient is given by:

$$\beta(z,\lambda) = \int_0^\infty Q_e(z,m,x)\pi r^2 \; n(z,r)\mathrm{d}r, \tag{2}$$

where Q_e is the Mie extinction efficiency factor, and is dependent on the Mie size parameter $x = 2\pi r/\lambda$, and the refractive index of the particles ($m = m_r + im_i$), $n(r)$ is the number size distribution.

The lognormal distribution is the most suitable representation for characterizing the size distribution of the atmospheric aerosols [4]. The distribution, in terms of number density as a function of radius $n(r)$, is described by its median radius (r_m), standard deviation (σ) of $\ln r$, and total number density (N_0):

$$n(r) = \frac{N_0}{\sqrt{2\pi}} \frac{1}{\sigma r} \; \exp\left[-\frac{(\ln r - \ln r_m)^2}{2\sigma^2}\right] \tag{3}$$

The primary source of aerosol properties used in the retrieval is the OPAC (Optical Properties of Aerosols and Clouds) database [11]. The database provides optical (most importantly, the complex refractive index as a function of wavelength) and physical properties (such as the size distribution and vertical distribution) for a set of aerosol components from which representative aerosol types can be built.

The quantity used to define the size of the aerosol particles in ORAC is the effective radius, defined as the the ratio of the third and second moments of the size distribution:

$$r_e = \frac{\int_0^\infty r^3 n(r) \; \mathrm{d}r}{\int_0^\infty r^2 n(r) \; \mathrm{d}r} \tag{4}$$

In order to produce radiance look-up tables from this database the scattering properties of each aerosol type are calculated. Scattering properties are calculated for the central wavelength of each channel across a range of effective radii from 0.02 to 20 μm. Two assumptions are made during this step:

- That the radiative properties of the aerosol are constant across the width of each instrument channel. As the features of aerosol extinction spectra are very broad in comparison with gas features this is a reasonable approximation.
- Assumptions must be made in determining both the form of the aerosol size distribution and how its shape varies with changing aerosol effective radius. To model aerosol distributions with different effective radii to those prescribed by the OPAC database, the relative concentration of the different-sized aerosol components which make up each aerosol class are changed. For example, if the effective radius needs to be decreased, the relative concentration of the smallest component of the aerosol (the accumulation mode) will be increased, while the larger components will be decreased.

If the required effective radius is equal to that given by the smallest or largest component of a given aerosol type, then the type effectively becomes a single component aerosol. If the size is outside of this range, then the mode radius of the smallest/largest components is shifted (while keeping the width of the component's distribution constant). Clearly, in such situations, the accuracy of the model can be called into question, so we are relying on the prescribed effective radius being relatively close to that found in the real world. It should also be pointed out that in the case of very small aerosol particles, the composition of the particles become less important in determining their scattering effects, since they will act more like Rayleigh scatterers.

These scattering properties are then used to generate a vertical profile of aerosol extinction and phase function, based on vertical profiles of number density, N:

$$N(z) = N(0)\exp(-z/Z), \tag{5}$$

where z is the height and Z is a scale height, defined by the aerosol type. For each layer at which the aerosol distribution is defined, the extinction coefficient, single scattering albedo and the coefficients of a Legendre expansion of the scattering phase function are calculated for each instrument channel and over 20 logarithmically spaced effective radii between 0.01 and 10 μm.

3.2 Modelling atmospheric gas absorption

Once aerosol scattering properties have been calculated, gas absorption over the instrument band passes is calculated in terms of an optical depth, and convolved with the instrument filter transmission functions, using MODTRAN [1]. MODTRAN provides tropical, mid-latitude summer and winter, subarctic summer and winter, and US Standard Atmosphere climatological atmospheres for the following gases: H_2O, CO_2, O_3, N_2O, CO, CH_4, plus single profiles for: HNO_3, NO, NO_2, SO_2, O_2, N_2, NH_3 and the heavy molecules (CFCs). ORAC look-up tables are generated using the mid-latitude summer atmosphere only. This simplification can be made as gas absorption is weak compared to aerosol extinction in the visible and the (A)ATSR channels are free from strong absorption features of gases which show large spatial and temporal variability (most notably, H_2O). Although the 1.6 μm channel of SEVIRI is slightly affected by H_2O, the effect on aerosol retrievals has been found to be negligible.

3.3 Modeling atmospheric transmission and reflectance

The final step in the FM is the prediction of atmospheric transmission and bi-directional reflectance, based on the aerosol phase functions and gas optical depth calculated in the previous two steps. The ORAC FM uses the DIscrete Ordinates Radiative Transfer (DISORT) software package [34] to perform this step.

The DISORT algorithm solves the equation for the transfer of monochromatic light at wavelength λ as described by the equation

$$\mu \frac{\mathrm{d}L_\lambda(\tau_\lambda, \mu, \phi)}{\mathrm{d}\tau} = L_\lambda(\tau_\lambda, \mu, \phi) - L^S_\lambda(\tau_\lambda, \mu, \phi), \tag{6}$$

where $L_\lambda(\tau_\lambda, \mu, \phi)$ is the intensity along direction μ, ϕ (where μ is the cosine of the zenith angle and ϕ is the azimuth angle) at optical depth τ_λ measured perpendicular to the surface of the medium. $L_\lambda^S(\tau_\lambda, \mu, \phi)$ is the source function.

It should be noted that DISORT still makes some important approximations, which can limit its accuracy in certain circumstances. The most important of these are:

- It assumes a plane parallel atmosphere, which makes it inapplicable at viewing or zenith angles above approximately 80°, where the curvature of the Earth has a significant influence on radiative transfer.
- It is a one-dimensional model, so cannot reproduce the effects of horizontal gradients in the scattering medium. This is important where strong gradients exist, such as near cloud edges.
- It does not model polarization effects and hence cannot be used to model measurements made by instruments which are sensitive to polarization and does not take the polarization introduced into the diffuse component of radiance by Rayleigh scattering.[2]

DISORT is provided with the aerosol-scattering properties defined by the Mie scattering calculations and the gas absorptions defined by MODTRAN and a series of 20 logarithmically spaced aerosol optical depths (defined at a wavelength of 0.55 μm) between 0.008 and 5.6. Although DISORT has the ability to include a surface of arbitrary reflectance 'below' the modeled atmosphere, no surface reflectance is included at this step. Rather, the transmission and reflectance of the atmosphere alone is computed for both direct beam and diffuse radiation sources separately. These calculations produce five look-up tables for each aerosol type/channel combination:

- Bidirectional reflectance of the atmosphere, from the top of the atmosphere, $R_{\mathrm{BD}}(\theta_0, \theta_\mathrm{v}, \phi)$.
- Diffuse reflectance of the atmosphere to diffuse radiance, from the bottom of the atmosphere, R_{FD}.
- Diffuse transmission of an incident beam, $T_{\mathrm{BD}}^{\downarrow}(\theta_0)$.
- Direct transmission of the beam, $T_{\mathrm{DB}}^{\downarrow}(\theta_0)$, or $T_{\mathrm{DB}}^{\uparrow}(\theta_\mathrm{v})$.
- Total transmission in the viewing direction, $T^{\uparrow}(\theta_\mathrm{v})$.

Here, a $\downarrow$ denotes transmission from the top to the bottom of the atmosphere, while $\uparrow$ indicates the reverse. θ_0, θ_v and ϕ indicate a dependence on the solar zenith, viewing zenith and relative azimuth angles, respectively. Each of these files contains tabulated transmission or reflectance (depending on the file) values for each of the twenty effective radii, nine 0.55 μm optical depths and sun/satellite geometry (specified by 20 equally spaced zenith angles and 11 equally spaced azimuth angles).

Effects of molecular absorption and Rayleigh scattering are included by adjustment of the layer's optical depth and the particle's single scattering albedo and phase function with the following:

$$\tau = \tau_\mathrm{a} + \tau_\mathrm{R} + \tau_\mathrm{g}, \tag{7}$$

$$\omega = \frac{\tau_\mathrm{R} + \omega_\mathrm{a}\tau_\mathrm{a}}{\tau_\mathrm{g} + \tau_\mathrm{R} + \tau_\mathrm{a}}, \tag{8}$$

[2] It should be noted that DISORT has now be superseded by the vectorized VDISORT code [31], which does include polarization effects. However, this code has yet to be implemented in the ORAC scheme.

$$P(\theta) = \frac{\tau_a \omega_a P_a(\theta) + \tau_R P_R(\theta)}{\tau_a \omega_a + \tau_R}, \tag{9}$$

where τ_a, τ_R and τ_g are the contributions to the total optical depth τ due to aerosol scattering, Rayleigh scattering and gaseous absorption within each layer respectively. The aerosol single scattering albedo is denoted ω_a.

For each layer bounded by lower and upper pressure levels p_l and p_u, respectively and ground-level pressure p_0, τ_R is calculated from

$$\tau_R = \frac{\tau_{RT}[p_l - p_u]}{p_0}, \tag{10}$$

where τ_{RT}, the wavelength-dependent Rayleigh scattering optical depth for a column of atmosphere extending from the ground surface to the top of the atmosphere, is obtained from [15]:

$$\tau_{RT}(\lambda) = \frac{p_0}{p_s} \times \frac{1}{117.03\lambda^4 - 1.316\lambda^2}, \tag{11}$$

where p_s is the standard pressure ($p_s = 1013.25$ hPa), p_0 is the ground pressure in hPa and λ is in μm.

4. Surface reflectance

Of crucial importance in the retrieval of aerosol properties from 'near-nadir' visible/near-infrared satellite measurements (i.e. measurements in which the Earth's surface contributes to the measured radiances) is an accurate description of the surface reflectance. Both the Lambertian and BRDF surface reflectance versions of ORAC retrieve the surface reflectance in addition to the aerosol optical depth and effective radius, however, it is still necessary to have accurate *a priori* knowledge of it.

The methodology used to produce an *a priori* surface reflectance differs between measurements made over sea or land. Over the sea a surface reflectance model based on the method presented by Koepke [17] is used. This model includes upwelling radiance from volume scattering within the water itself [22], specular reflections from the wind-roughened surface (as modeled by the Cox and Munk method [4, 5]) and reflection from white caps [21, 23]. The model uses ECMWF reanalysis wind fields to determine wave statistics and white cap coverage and can also make use of chlorophyll concentrations and gelbstoff loading from MERIS products. A detailed description of the model is given by Sayer [30].

Over land the MODIS[3] land surface bidirectional reflectance product [14] is used to define the *a priori* surface reflectance. The product consists of a set of three parameters for the MODIS AMBRALS (Algorithm for Modelling Bidirectional Reflectance Anisotropies of the Land Surface) surface reflectance model [36], which itself consists of three simple reflectance kernels for different surface types:

[3] MODerate resolution Imaging Spectrometer.

- Isotropic kernel. Lambertian reflectance, for which the kernel is $\equiv 1$.
- Ross-thick kernel, $K_{\mathrm{Rt}}(\theta_0, \theta_\mathrm{v}, \phi)$. Parameterizes densely packed, randomly oriented reflectors, such as leaves.
- Li-sparse kernel, $K_{\mathrm{Li}}(\theta_0, \theta_\mathrm{v}, \phi)$. Parameterizes the shadowing effects of isolated large objects, such as scattered trees.

The three coefficients, p_{iso}, p_{vol} and p_{geo} for the isotropic, Ross-thick and Li-sparse kernels respectively, provided by the BRDF product weight these models to reproduce the atmospherically corrected bi-directional surface reflectance observed by MODIS over a 16-day period.

The MODIS BRDF product has as specified uncertainty of ± 0.02 in the white sky albedo derived from the AMBRALS model coefficients. Validation work [13, 28] has shown this to be a reasonable estimate of the true accuracy of the product in general, although accuracy can decrease for scenes with a highly heterogeneous surface.

Since the Ross-thick and Li-sparse kernels are both dependent only on the solar and viewing directions, the AMBRALS model can be written in the form:

$$R_{\mathrm{SBD}} = p_{\mathrm{iso}} + K_{\mathrm{Rt}}(\theta_0, \theta_\mathrm{v}, \phi)p_{\mathrm{vol}} + K_{\mathrm{Li}}(\theta_0, \theta_\mathrm{v}, \phi)p_{\mathrm{geo}}. \tag{12}$$

These coefficients can also be combined to form either a black-sky albedo:

$$R_{\mathrm{SLB}} = p_{\mathrm{iso}} + \left(b_{\mathrm{bs1}} + b_{\mathrm{bs2}}\theta_0^2 + b_{\mathrm{bs3}}\theta_0^3\right)p_{\mathrm{vol}} + \left(c_{\mathrm{bs1}} + c_{\mathrm{bs2}}\theta_0^2 + c_{\mathrm{bs3}}\theta_0^3\right)p_{\mathrm{geo}}, \tag{13}$$

or a white-sky albedo:

$$R_{\mathrm{SLW}} = p_{\mathrm{iso}} + b_{\mathrm{ws}}p_{\mathrm{vol}} + c_{\mathrm{ws}}p_{\mathrm{geo}}, \tag{14}$$

where the quantities b_{ws}, c_{ws}, b_{bs1}, etc. are constant coefficients published by the MODIS BRDF team [32].

Sunglint

A major problem encountered in making nadir satellite measurements is the specular reflection of sunlight off the ocean surface, usually referred to as sunglint. Sunglint has two detrimental impacts:

1. The TOA signal becomes dominated by the directly reflected radiance from the surface.
2. Consequently, the Lambertian surface reflectance approximation (usually valid for the ocean surface) becomes wholly inadequate. For these reasons, a retrieval using the Lambertian Fast-FM (see Section 5) will not produce accurate results in regions of sunglint and they must be masked out, resulting in significant loss of data. The BRDF forward model is able to successfully model the radiative transfer in sun-glint regions. However, it becomes highly dependeant on accurate modeling of the surface reflectance (which in turn depends on the accuracy of the assumed surface wind conditions), due to the relatively small contribution of the atmosphere to TOA radiance in these regions.

5. The Lambertian fast forward model

The Fast-FM uses the transmission and reflectance look-up tables produced by the FM to predict a top-of-atmosphere radiance using the scheme shown diagrammatically in Fig. 7.1. The solar beam is incident on the atmosphere and the first contribution to the TOA observed radiance is the direct bi-directional reflectance, R_{BD}, of the atmosphere. Transmission through the atmosphere is partly by direct transmission of the beam, $T^{\downarrow}_{\mathrm{DB}}$, and partly by diffuse transmission of scattered radiance, $T^{\downarrow}_{\mathrm{BD}}$. As an underlying Lambertian surface is assumed, any preferred directionality of the radiance is lost on reflection and these transmitted terms can be combined to give the total transmission downward through the atmosphere, $T^{\downarrow} = T^{\downarrow}_{\mathrm{BD}} + T^{\downarrow}_{\mathrm{DB}}$. Radiation reflected by the surface (with reflectance R_{s}) is partially transmitted by the atmosphere into the viewing direction. This transmission, again with the direct and diffuse components combined, is denoted by $T^{\uparrow}$. The atmosphere also reflects downwards (with reflectance R_{FD}) so there is a set of multiple reflections and transmissions giving rise to a series of rapidly decreasing contributions to the TOA reflectance. This process is represented in the following equation:

$$\begin{aligned} R(\theta_0,\theta_{\mathrm{v}},\phi) = R_{\mathrm{BD}}(\theta_0,\theta_{\mathrm{v}},\phi) &+ T^{\downarrow}(\theta_0)R_{\mathrm{s}}T^{\uparrow}(\theta_{\mathrm{v}}) \\ &+ T^{\downarrow}(\theta_0)R_{\mathrm{s}}^2T^{\uparrow}(\theta_{\mathrm{v}})R_{\mathrm{FD}} \\ &+ T^{\downarrow}(\theta_0)R_{\mathrm{s}}^3T^{\uparrow}(\theta_{\mathrm{v}})R_{\mathrm{FD}}^2 \\ &+ \ldots . \end{aligned} \tag{15}$$

This expression can be simplified to give

$$R(\theta_0,\theta_{\mathrm{v}},\phi) = R_{\mathrm{BD}}(\theta_0,\theta_{\mathrm{v}},\phi) + T^{\downarrow}(\theta_0)R_{\mathrm{s}}T^{\uparrow}(\theta_{\mathrm{v}})\left(1 + R_{\mathrm{s}}R_{\mathrm{FD}} + R_{\mathrm{S}}^2R_{\mathrm{FD}}^2 + \ldots\right) \tag{16}$$

which, in turn, can be simplified further in terms of a geometric series limit,

$$R(\theta_0,\theta_{\mathrm{v}},\phi) = R_{\mathrm{BD}}(\theta_0,\theta_{\mathrm{v}},\phi) + \frac{T^{\downarrow}(\theta_0)T^{\uparrow}(\theta_{\mathrm{v}})R_{\mathrm{s}}}{1 - R_{\mathrm{s}}R_{\mathrm{FD}}}. \tag{17}$$

It is this equation that is used to calculate the top-of-atmosphere radiances seen by the satellite.

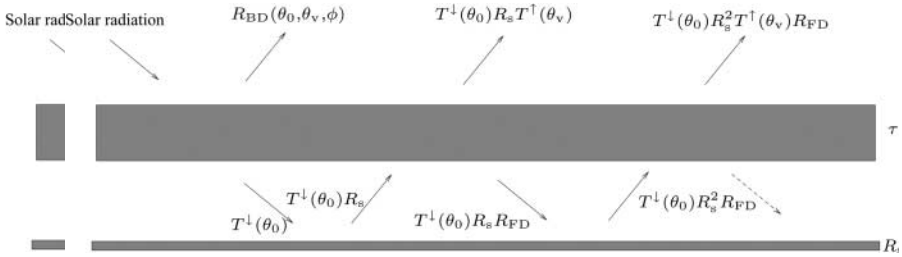

Fig. 7.1. Atmosphere surface interactions.

5.1 Forward model gradient

The gradient of the forward model $(\partial y/\partial x)$ where y is a radiance measurement in a single channel and x is one of the state variables is required for the following two purposes:

1. The gradient with respect to parameters which are to be derived from the measurements (state parameters) is a vital quantity for the inversion of the non-linear reflectance model by the Levenberg–Marquardt algorithm.
2. The gradient with respect to parameters which might be considered known and not part of the inversion procedure (model parameters), e.g., surface reflectance spectral shape, is used to judge the sensitivity to these parameters and thus to estimate their contribution to the retrieval error.

If Eq. (17) is rewritten as

$$R = R_{\mathrm{BD}} + S, \tag{18}$$

then without reproducing the algebra it can be simply stated that the gradient of the model with respect to optical depth or effective radius is given by:

$$\frac{\partial R}{\partial x} = R'_{\mathrm{BD}} + S\left(\frac{T^{\downarrow}T^{\uparrow\prime} + T^{\downarrow\prime}T^{\uparrow}}{T^{\downarrow}T^{\uparrow}} + \frac{R_{\mathrm{S}}R'_{\mathrm{FD}}}{1 - R_{\mathrm{S}}R_{\mathrm{FD}}}\right) \tag{19}$$

where all $'$ indicate $\partial/\partial x$ and x is either τ or r_{e}.

The gradient with respect to surface reflectance is given by:

$$\frac{\partial R}{\partial R_{\mathrm{s}}} = \frac{T^{\downarrow}T^{\uparrow}}{\left(1 - R_{\mathrm{s}}R_{\mathrm{FD}}\right)^2}. \tag{20}$$

6. The BRDF fast forward model

Although the approximation of a Lambertian surface reflectance is reasonable for many surface types, it can be grossly inaccurate in some situations. For this reason a new Fast-FM has been developed for the ORAC retrieval system that, while using the same reference forward model and look-up tables as the Lambertian forward model, no longer makes this assumption. Dropping the assumption of a Lambertian surface reflectance has two consequences on the derivation of the Fast-FM:

1. The surface reflectance can no longer be described by one value. Rather, three values are required:
   - A bi-direction reflectance, R_{SBD}, is needed to characterize the reflection of the direct solar beam into the viewing angle. This is a function of both solar and viewing angles.
   - An equivalent black-sky albedo, or hemispherical reflectance, R_{SLB}, is needed to characterize the diffuse reflection of the direct beam over the whole hemisphere. This is only a function of the solar angle.
   - An equivalent white-sky albedo, or bi-hemispherical reflectance, R_{SLW}, is needed to characterize the reflection of diffuse downwelling radiation. This is independent of solar and viewing angles, since it assumes reflection is isotropic.
2. The combination of the direct transmission of the solar beam, $T^{\downarrow}_{\mathrm{DB}}$, and the diffuse transmission of the scattered radiance from the solar beam, $T^{\downarrow}_{\mathrm{BD}}$, into a single term

$T^{\downarrow}$ is no longer possible, because the direct beam and diffuse radiance are subject to different reflectances at the ground.

This means Eq. (15) becomes:

$$
\begin{aligned}
R(\theta_0,\theta_v,\phi) = R_{BD}(\theta_0,\theta_v,\phi) &+ T^{\downarrow}_{DB}(\theta_0)R_{SBD}(\theta_0,\theta_v,\phi)T^{\uparrow}_{DB}(\theta_v) \\
&+ T^{\downarrow}_{DB}(\theta_0)R_{SLB}(\theta_0)\left(T^{\uparrow}(\theta_v) - T^{\uparrow}_{DB}(\theta_v)\right) \\
&+ T^{\downarrow}_{BD}(\theta_0)R_{SLW}T^{\uparrow}(\theta_v) \\
&+ T^{\downarrow}_{DB}(\theta_0)R_{SLB}(\theta_0)R_{FD}R_{SLW}T^{\uparrow}(\theta_v) \\
&+ T^{\downarrow}_{BD}(\theta_0)R_{SLW}R_{FD}R_{SLW}T^{\uparrow}(\theta_v) \\
&+ T^{\downarrow}_{DB}(\theta_0)R_{SLB}(\theta_0)R_{FD}R_{SLW}R_{FD}R_{SLW}T^{\uparrow}(\theta_v) \\
&+ T^{\downarrow}_{BD}(\theta_0)R_{SLW}R_{FD}R_{SLW}R_{FD}R_{SLW}T^{\uparrow}(\theta_v) \\
&+ \ldots.
\end{aligned}
\tag{21}
$$

Here the term $T^{\downarrow}_{DB}(\theta_0)R_{SBD}(\theta_0,\theta_v,\phi)T^{\uparrow}_{DB}(\theta_v)$ is the direct reflection of the solar beam into the viewing angle at the surface and thus uses the transmission of the direct beam for both the downward and upward paths through the atmosphere. $T^{\downarrow}_{DB}(\theta_0)R_{SLB}(\theta_0)\left(T^{\uparrow}(\theta_v) - T^{\uparrow}_{DB}(\theta_v)\right)$ is the diffuse reflection of the direct beam, i.e. it is the radiance seen at the satellite due to the direct beam being diffusely scattered by the ground. Note that for this term, the upwelling transmission is the total transmission minus the direct beam transmission, since we are only interested in the diffuse component. Together, these two terms are equivalent to the $T^{\downarrow}_{DB}(\theta_0)R_S T^{\uparrow}(\theta_v)$ term present in the Lambertian forward model. Notice also that we require the diffuse-only transmission for the upwelling radiation from the black-sky ($R_{SLB}(\theta_0)$) term.

The term $T^{\downarrow}_{BD}(\theta_0)R_{SLW}T^{\uparrow}(\theta_v)$ approximates the reflection of the diffusely transmitted solar radiation into the viewing direction. Ideally, this would be split into two terms: $T^{\downarrow}_{BD}(\theta_0)R_{SLW}T^{\uparrow}_{BD}(\theta_v) + T^{\downarrow}_{BD}(\theta_0)R_{SLB}(\theta_v)T^{\uparrow}_{DB}(\theta_v)$, where the first gives the upward diffuse transmission to the satellite and the second gives the direct transmission. By setting $R_{SLB}(\theta_v) = R_{SLW}$ these two terms combine to give the above expression and $R_{SLB}(\theta_v)$ can be eliminated from the equation. This greatly simplifies the formulation of the forward model and reduces the number of values which must be propogated through the retrieval by one. The rest of the terms in Eqn.(21) are multiple surface–atmosphere reflections, analogous to those which appear in the Lambertian forward model.

This model makes two simplifying assumptions:

1. The combining of the upwelling direct and diffuse components of the reflected diffusely transmitted solar radiation described above amounts to the approximation that the surface acts as a Lambertian reflector when diffusely illuminated. That is to say that the surface will appear the same from all viewing directions if lit by a purely diffuse source.
2. We also assume that when taken as a pair, the surface and atmosphere act as Lambertian reflectors, so that any directionality left the reflected beam ($T^{\downarrow}_{DB}(\theta_0)R_{SBD}(\theta_0,\theta_v,\phi)$) is lost in that proportion which is reflected back towards the ground.

Following on from this approximation, after the first surface-atmosphere pair of reflections, the radiation has lost all directionality, and thus the white sky albedo is used for

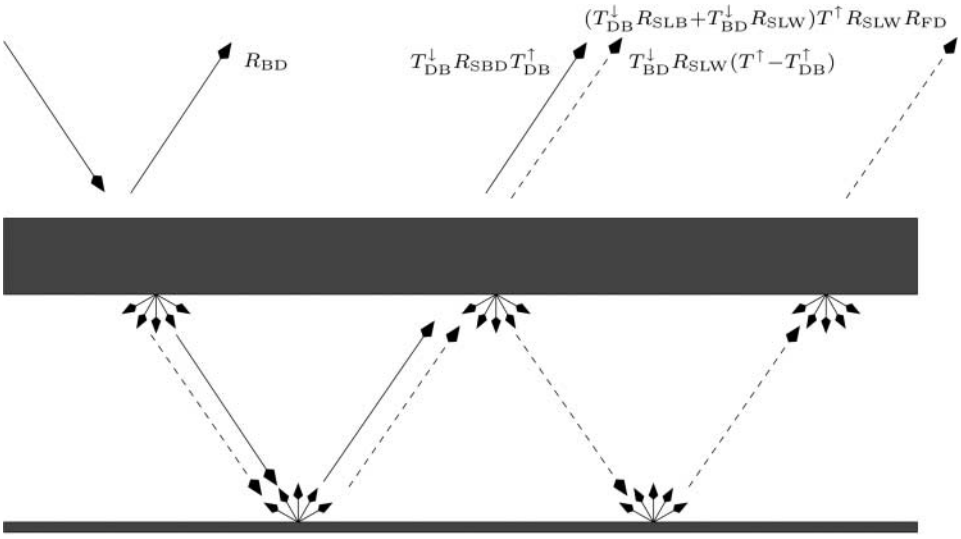

Fig. 7.2. Atmospher–surface interactions using the simplified BRDF model.

subsequent surface reflections, and the total atmospheric transmission ($T^{\uparrow}(\theta_{\mathrm{v}})$) for the final upward transmission (Fig. 7.2).

Again, Eq. (21) can be simplified:

$$\begin{aligned} R(\theta_0,\theta_{\mathrm{v}},\phi) = {} & R_{\mathrm{BD}}(\theta_0,\theta_{\mathrm{v}},\phi) + T^{\downarrow}_{\mathrm{DB}}(\theta_0)R_{\mathrm{SBD}}(\theta_0,\theta_{\mathrm{v}},\phi)T^{\uparrow}_{\mathrm{DB}}(\theta_{\mathrm{v}}) \\ & - T^{\downarrow}_{\mathrm{DB}}(\theta_0)R_{\mathrm{SLB}}(\theta_0)T^{\uparrow}_{\mathrm{DB}}(\theta_{\mathrm{v}}) \\ & + \Big(T^{\downarrow}_{\mathrm{DB}}(\theta_0)R_{\mathrm{SLB}}(\theta_0) + T^{\downarrow}_{\mathrm{BD}}(\theta_0)R_{\mathrm{SLW}}\Big)T^{\uparrow}(\theta_{\mathrm{v}}) \\ & \big(1 + R_{\mathrm{SLW}}R_{\mathrm{FD}} + R^2_{\mathrm{SLW}}R^2_{\mathrm{FD}} + \ldots\big). \end{aligned} \tag{22}$$

Applying the same series limit as before, our new reflectance value is given by:

$$\begin{aligned} R(\theta_0,\theta_{\mathrm{v}},\phi) = {} & R_{\mathrm{BD}}(\theta_0,\theta_{\mathrm{v}},\phi) + T^{\downarrow}_{\mathrm{DB}}(\theta_0)(R_{\mathrm{SBD}}(\theta_0,\theta_{\mathrm{v}},\phi) - R_{\mathrm{SLB}}(\theta_0))T^{\uparrow}_{\mathrm{DB}}(\theta_{\mathrm{v}}) \\ & + \frac{\Big(T^{\downarrow}_{\mathrm{DB}}(\theta_0)R_{\mathrm{SLB}}(\theta_0) + T^{\downarrow}_{\mathrm{BD}}(\theta_0)R_{\mathrm{SLW}}\Big)T^{\uparrow}(\theta_{\mathrm{v}})}{1 - R_{\mathrm{SLW}}R_{\mathrm{FD}}}. \end{aligned} \tag{23}$$

6.1 Retrieving the surface reflectance with the BRDF forward model

Using the Lambertian surface forward model, the magnitude of the surface reflectance (in particular, the albedo at 0.55 μm) is retrieved. The spectral shape of the surface reflectance (i.e. the ratios between the reflectance in different channels) is fixed by the *a priori* surface albedo (from the MODIS white-sky albedo over land and from the surface reflectance model over the ocean), but the magnitude of this reflectance is allowed to vary. When using the BRDF forward model we are faced with having three separate re-

flectances for each channel. How then do we include the surface reflectance as a retrieved parameter?

As has been described already, the black-sky albedo describes the amount of radiation scattered into the entire hemisphere for a single incoming beam at a given zenith angle. Hence it can be derived from the BRDF:

$$R_{\mathrm{SLB}}(\theta_0) = \frac{\int_0^{2\pi}\int_0^{\pi/2} R_{\mathrm{SBD}}(\theta_0,\theta_{\mathrm{v}},\phi)\cos\theta_{\mathrm{v}}\sin\theta_{\mathrm{v}}\ \mathrm{d}\theta_{\mathrm{v}}\ \mathrm{d}\phi}{\int_0^{2\pi}\int_0^{\pi/2}\cos\theta_{\mathrm{v}}\sin\theta_{\mathrm{v}}\ \mathrm{d}\theta_{\mathrm{v}}\ \mathrm{d}\phi} \tag{24}$$

$$= \frac{1}{\pi}\int_0^{2\pi}\int_0^{\pi/2} R_{\mathrm{SBD}}(\theta_0,\theta_{\mathrm{v}},\phi)\cos\theta_{\mathrm{v}}\sin\theta_{\mathrm{v}}\ \mathrm{d}\theta_{\mathrm{v}}\ \mathrm{d}\phi.$$

Similarly the white-sky albedo is the amount of light scattered over the entire hemisphere from isotropic diffuse downwelling radiance. It can be calculated by integrating R_{SLB} across all solar zenith angles:

$$R_{\mathrm{SLW}} = \frac{\int_0^{\pi/2} R_{\mathrm{SLB}}(\theta_0)\cos\theta_0\sin\theta_0 \mathrm{d}\theta_0}{\int_0^{\pi/2}\cos\theta_{\mathrm{v}}\sin\theta_{\mathrm{v}}\ \mathrm{d}\theta_0} = 2\int_0^{\pi/2} R_{\mathrm{SLB}}(\theta_0)\cos\theta_0\sin\theta_0\ \mathrm{d}\theta_0. \tag{25}$$

It is clear from these two equations that a small change in any one of the three surface reflectance values will result in a proportional change in the other two, since a constant can simply be moved outside the integral.

Examining Eq. (12), (13) and (14) for the calculation of bi-directional reflectance, black-sky albedo and white-sky albedo from the MODIS BRDF product, it can be seen that, for a given pixel, we have three linear equations of the form

$$R = p_{\mathrm{iso}} + c_1 p_{\mathrm{vol}} + c_2 p_{\mathrm{geo}}. \tag{26}$$

Hence the reflectances calculated using these expressions also scale linearly.

The ORAC BRDF retrieval is set up to treat the white-sky albedo as the retrieved parameter, with the bi-directional and black-sky albedo values being derived from it, as the white-sky albedo is independent of the viewing geometry.

6.2 Derivatives of the forward model expression

The derivative of Eq. (23) with respect to optical depth or effective radius can be shown to be

$$\begin{aligned}\frac{\partial R}{\partial x} = {} & R'_{\mathrm{BD}} + (R_{\mathrm{SBD}} - R_{\mathrm{SLB}})\left(T^{\downarrow}_{\mathrm{DB}}T'^{\uparrow}_{\mathrm{DB}} + T'^{\downarrow}_{\mathrm{DB}}T^{\uparrow}_{\mathrm{DB}}\right) \\ & + \frac{\left(T^{\downarrow}_{\mathrm{DB}}R_{\mathrm{SLB}} + T^{\downarrow}_{\mathrm{BD}}R_{\mathrm{SLW}}\right)R_{\mathrm{SLW}}T^{\uparrow}R'_{\mathrm{FD}}}{\left(1 - R_{\mathrm{SLW}}R_{\mathrm{FD}}\right)^2} \\ & + \frac{\left(T^{\downarrow}_{\mathrm{DB}}R_{\mathrm{SLB}} + T^{\downarrow}_{\mathrm{BD}}R_{\mathrm{SLW}}\right)T'^{\uparrow} + T^{\uparrow}\left(R_{\mathrm{SLW}}T'^{\downarrow}_{\mathrm{BD}} + R_{\mathrm{SLB}}T'^{\downarrow}_{\mathrm{DB}}\right)}{1 - R_{\mathrm{SLW}}R_{\mathrm{FD}}},\end{aligned} \tag{27}$$

where all $'$ indicate $\partial/\partial x$ and x is either τ or r_{e}.

The derivative with respect to surface reflectance requires that we express the derivatives of R_{SBD} and R_{SLB} in terms of a derivative of R_{SLW}. Since R_{SBD} and R_{SLB} both depend linearly on R_{SLW} for a given viewing geometry, we can write:

$$\frac{\partial R}{\partial R_{SBD}} = \frac{\partial R}{\partial R_{SLW}} \frac{\partial R_{SLW}}{\partial R_{SBD}} = \frac{1}{\alpha} \frac{\partial R}{\partial R_{SLW}} \tag{28}$$

$$\frac{\partial R}{\partial R_{SLB}} = \frac{\partial R}{\partial R_{SLW}} \frac{\partial R_{SLW}}{\partial R_{SLB}} = \frac{1}{\beta} \frac{\partial R}{\partial R_{SLW}}, \tag{29}$$

and the derivative can then be expressed as:

$$\frac{\partial R}{\partial R_{SLW}} = T_{DB}^{\downarrow}(\alpha\beta)T_{DB}^{\uparrow} + \frac{T_{DB}^{\downarrow}\beta T^{\uparrow} + T_{BD}^{\downarrow} T^{\uparrow}}{1 - R_{SLW}R_{FD}} + \frac{\left(T_{DB}^{\downarrow}R_{SLB} + T_{BD}^{\downarrow}R_{SLW}\right)T^{\uparrow}}{\left(1 - R_{SLW}R_{FD}\right)^2}. \tag{30}$$

7. The thermal infrared forward model

In general aerosol has a relatively small impact on the TOA radiance in the thermal infrared, as the particles are generally small enough to act as Rayleigh scatters at these wavelengths (i.e. the aerosol signal becomes lost in the Planck curve of the atmosphere). However, large particles, such as wind-blown dust, can have a significant thermal infrared signature. This fact has been widely used to develop dust indices, such as the Saharan Dust Index (SDI) [19] used with SEVIRI. The potential of thermal information on wind-blown dust is especially great in situations where the lofted dust is above surfaces with a similar composition. In such cases the contrast between the aerosol and surface in the visible/near-infrared is particularly poor. However, thermal channels show a strong contrast, as the lofted dust is almost universally at a significantly lower temperature than the surface.

In order to take advantage of this potential, a version of the ORAC aerosol retrieval which can utilize thermal window channels,[4] has been developed. Using the thermal channels complicates the retrieval scheme in four main ways:

1. A separate Fast-FM is required for thermal channels, as their signal is dominated by thermal emission from the Earth's surface and atmosphere, rather than scattering and reflection of solar radiation.
2. In window channels, the thermal signal is dominated by the surface temperature and emissivity. Thus, these parameters must also be accounted for in the retrieval.
3. In order to accurately model the TOA brightness temperature, the thermal emission of the atmosphere without aerosol loading (i.e. clear-air) must also be modeled. This involves further radiative transfer calculations and requires accurate knowledge of the temperature structure and trace-gas concentrations of the atmosphere.
4. Since the thermal emission of the aerosol depends on its altitude, this must be accounted for in the retrieval.

[4] Channels for which the signal from trace gas absorption and emission is low and the signal is dominated by the thermal emission from the ground and atmosphere.

In order to model the clear-sky brightness temperature, RTTOV [25, 29] is used in conjunction with ECMWF reanalysis data for the scene of interest. The ECMWF fields used are the surface temperature and pressure, and profiles of temperature, humidity and ozone. ECMWF data are available at 6-hour intervals, and are linearly interpolated to the measurement time of the satellite. Clearly, the lack of any trace gas information in the ECMWF data, aside from water vapor and ozone, means this approach will only be valid for instrument channels where there is little signal from gas absorption or emission lines (i.e. the analysis is limited to making use of window channels). RTTOV provides the temperature at 43 layers, the transmission from the surface to each layer and from each layer to the TOA, as well as the upwelling and downwelling clear-sky radiance at each level, for each pixel in the satellite image to analysed.

In the calculation of aerosol look-up tables, it is necessary to extend the calculation of transmission and reflectance of the aerosol layer to diffuse radiation to the thermal wavelengths, as well as calculating its emissivity (values for the direct beam transmission and bi-directional reflectance are not required, as there is no direct beam component in the thermal radiative transfer). Thus, aerosol optical properties are required which extend into the thermal infrared.

Additionally the dependence of the thermal signal on the height distribution of the aerosol must be accounted for. In the generation of the look-up tables, the aerosol is modelled as a single infinitesimally thin layer, for which the transmission, reflectance and emissivity are computed. In the retrieval, the height of this layer is variable (i.e. the layer height is a retrieved parameter), and is assumed to be in thermal equilibrium with the surrounding atmosphere. This approximation will only be valid in certain circumstances (i.e. where a single elevated aerosol layer exists). However, in the case of wind-blown dust, this is a common scenario (see [18] for example). Simulations have shown that grossly different aerosol height distributions (such as boundary layer aerosol below an elevated layer or aerosol across a broad height range) lead to errors in retrieved parameters which are similar to, or significantly smaller than the expected error due to uncertainty in the measured radiances.

Derivation of the thermal Fast-FM follows a similar pattern to that of the shortwave Fast-FM. If we define:

- Upwelling TOA radiance, $I^{\uparrow}$.
- Transmission of the atmosphere above the aerosol layer, T_{al}.
- Upwelling TOA radiance from the atmosphere above the aerosol layer, $I^{\uparrow}_{\mathrm{al}}$.
- Downwelling radiance at the top the aerosole layer from the overlying atmosphere, $I^{\downarrow}_{\mathrm{al}}$.
- Transmission of the atmosphere below the aerosol layer, T_{bl}.
- Upwelling radiance at the bottom of the aerosol layer neglecting multiple reflection, between the layer and underlying surface, $I^{\uparrow}_{\mathrm{bl}}$.
- Black body radiance at of the aerosol layer, B_{l}.
- Emissivity of the aerosol layer, ε_{l}.
- Reflectance of the aerosol layer, R_{l}.
- Surface reflectance, R_{s}.

The TOA thermal intensity can then be expressed as

$$I^{\uparrow} = B_{\mathrm{l}}\varepsilon_{\mathrm{l}}T_{\mathrm{al}} + I^{\downarrow}_{\mathrm{al}}R_{\mathrm{l}}T_{\mathrm{al}} + I^{\uparrow}_{\mathrm{al}} + I^{\uparrow}_{\mathrm{bl}}T_{\mathrm{l}}T_{\mathrm{al}} + I^{\uparrow}_{\mathrm{bl}}R_{\mathrm{l}}T^{2}_{\mathrm{bl}}R_{\mathrm{s}}T_{\mathrm{l}}T_{\mathrm{al}} + I^{\uparrow}_{\mathrm{bl}}R^{2}_{\mathrm{l}}T^{4}_{\mathrm{bl}}R^{2}_{\mathrm{s}}T_{\mathrm{c}}T_{\mathrm{a}}l + \ldots. \quad (31)$$

Here the first term is the thermal emission from the aerosol layer itself, the second term gives the contribution from downwelling radiance reflected by the aerosol layer and the third and fourth terms are the contribution from thermal emission of the atmosphere above and below the aerosol layer, respectively. The remaining terms account for multiple reflections between the surface and the aerosol layer. As with the shortwave forward model, this expression can be simplified by factorizing and applying a geometric series limit:

$$I^{\uparrow} = B_{\mathrm{l}}\varepsilon_{\mathrm{l}}T_{\mathrm{al}} + I_{\mathrm{al}}^{\downarrow}R_{\mathrm{l}}T_{\mathrm{al}} + I_{\mathrm{al}}^{\uparrow} + I_{\mathrm{bl}}^{\uparrow}T_{\mathrm{l}}T_{\mathrm{al}}\left(1 + R_{\mathrm{l}}T_{\mathrm{bl}}^{2}R_{\mathrm{s}} + R_{\mathrm{l}}^{2}T_{\mathrm{bl}}^{4}R_{\mathrm{s}}^{2} + \ldots\right), \tag{32}$$

leading to the expression

$$I^{\uparrow} = B_{\mathrm{l}}\varepsilon_{\mathrm{l}}T_{\mathrm{al}} + I_{\mathrm{al}}^{\downarrow}R_{\mathrm{l}}T_{\mathrm{al}} + I_{\mathrm{al}}^{\uparrow} + \frac{I_{\mathrm{bl}}^{\uparrow}T_{\mathrm{l}}T_{\mathrm{al}}}{1 - R_{\mathrm{l}}T_{\mathrm{bl}}^{2}R_{\mathrm{s}}}. \tag{33}$$

Note that the value $I_{\mathrm{bl}}^{\uparrow}$ includes both the atmospheric transmission below the aerosol layer and emission from the surface:

$$I_{\mathrm{bl}}^{\uparrow} = I_{\mathrm{bl}}^{\uparrow(atm)} + B_{\mathrm{s}}\varepsilon_{\mathrm{s}}T_{\mathrm{bl}}, \tag{34}$$

where B_{s} is the blackbody radiance of the surface and ε_{s} is its emissivity.

If we neglect multiple scattering between the surface and aerosol layer (which is a reasonable approximation at thermal wavelengths), the later terms in Eq. (31) and (32) become zero and the denominator of Eq. (32) becomes unity.[5] Applying this approximation and substituting (34), we get:

$$I^{\uparrow} = B_{\mathrm{l}}\varepsilon_{\mathrm{l}}T_{\mathrm{al}} + I_{\mathrm{al}}^{\downarrow}R_{\mathrm{l}}T_{\mathrm{al}} + I_{\mathrm{al}}^{\uparrow} + B_{\mathrm{s}}\varepsilon_{\mathrm{s}}T_{\mathrm{bl}}T_{\mathrm{l}}T_{\mathrm{al}} + I_{\mathrm{bl}}^{\uparrow(atm)}T_{\mathrm{l}}T_{\mathrm{al}}. \tag{35}$$

In order to account for the height dependence of the aerosol thermal emission and the surface-temperature dependence, both of these quantities are retrieved by the thermal algorithm. The state vector for the thermal retrieval thus consists of:

- Aerosol optical depth at 0.55 μm.
- Aerosol effective radius.
- Surface albedo at 0.55 μm.
- Aerosol layer height.
- Surface temperature.

Due to the greatly extended spectral range encompassed when thermal channels are included in the retrieval, accurate knowledge of the aerosol spectral refractive index is even more essential than in a visible near-infrared algorithm. A case study carried out by Carboni et al. [3], showed that dust-like aerosol models currently available from the literature [6, 11] could not be used to reproduce radiances observed by SEVIRI over the Sahara Desert and Atlantic Ocean during a dust storm event. The errors in aerosol optical depth and effective radius from retrievals using these refractive indices were completely dominated by this discrepancy. More success was achieved using refractive indices from in-house spectral measurements of Saharan dust samples [24], however, there remain discre-

[5] Note that this is in effect the same as assuming a zero surface reflectance.

pancies that show the need for future improvement of the characterization of aerosol and the Earth's surface in the IR.

8. The retrieval algorithm

All three of the Fast-FMs described in the previous section fit into the same basic ORAC retrieval algorithm, with minor changes to deal with differing input variables (such as the necessity of dealing with three surface reflectance values for each pixel for a retrieval using the BRDF forward model). The algorithm is built around the optimal estimation framework described by Rogers [26, 27]. If we define the vector made up of the retrieved parameters to be the state vector, $\mathbf{x}$, and the a vector of the measurements, $\mathbf{y}$, then the probability density function of the state subject to the measurements is defined, by application of Bayes' theorem and Gaussian statistics, to be

$$-2\ln P(\mathbf{x}|\mathbf{y}) = (\mathbf{y}-\mathbf{F}(\mathbf{x}))\mathbf{S}_{\varepsilon}^{-1}(\mathbf{y}-\mathbf{F}(\mathbf{x})) + (\mathbf{x}-\mathbf{x}_{\mathrm{a}})\mathbf{S}_{\mathrm{a}}^{-1}(\mathbf{x}\mathbf{x}_{\mathrm{a}}). \tag{36}$$

Here $\mathbf{F}(\mathbf{x})$ is the forward function (i.e. the function which maps the state parameters to measurements, which we approximate with a forward model $\mathbf{f}(\mathbf{x})$), $\mathbf{S}_{\varepsilon}$ is the measurement error covariance matrix, $\mathbf{x}_{\mathrm{a}}$ is the *a priori* state vector and $\mathbf{S}_{\mathrm{a}}$ is the *a priori* error covariance matrix. Together $\mathbf{x}_{\mathrm{a}}$ and $\mathbf{S}_{\mathrm{a}}$ denote our best guess at the state before the measurement is made and the precision of this guess. The retrieval problem is, therefore, that of finding the minimum value of Eq. (36), which is known as the cost function (i.e. maximizing the probability of $\mathbf{x}$ subject to $\mathbf{y}$), which is known as the cost function.

ORAC uses the Levenberg–Marquardt numerical optimization to perform this minimization. This is an iterative procedure, whereby, if the number of measurements in $\mathbf{y}$ is m, and there are n state parameters, $\mathbf{x}$ is incremented by

$$\mathbf{x}_{i+1} = \mathbf{x}_i + \left(\mathbf{S}_{\mathrm{a}}^{-1} + \mathbf{K}_i^T\mathbf{S}_{\varepsilon}^{-1}\mathbf{K}_i + \gamma\mathbf{D}_n\right)^{-1}\left[\mathbf{K}_i^T\mathbf{S}_{\varepsilon}^{-1}(\mathbf{y}-\mathbf{F}(\mathbf{x})) - \mathbf{S}_{\mathrm{a}}^{-1}(\mathbf{x}-\mathbf{x}_{\mathrm{a}})\right], \tag{37}$$

where $\mathbf{K}$ is the weighting function matrix, γ is variable parameter, $\mathbf{D}_n$ is a $n \times n$ diagonal scaling matrix and the i subscript denotes values for the current iteration. $\mathbf{K}$ is a $m \times n$ matrix, with each column containing the derivative of the forward model with respect to each state parameter, i.e.

$$k_{i,j} = \frac{\partial f_i(\mathbf{x})}{\partial x_j}. \tag{38}$$

Thus, for a linear system, we could write $\mathbf{y} = \mathbf{K}\mathbf{x}$.

The parameter γ is the key to the efficiency and robustness of the Levenberg–Marquardt algorithm. If $\gamma \to \infty$, Eq. (37) tends to the step given by the steepest descent algorithm, which will always lie in the direction of the local 'downhill' gradient and is therefore very robust. If $\gamma \to 0$, however, the algorithm behaves like Gauss–Newton iteration, which, although less numerically robust than steepest descent, will provide an exact solution to a linear problem in one iteration. The procedure for determining the value of γ is to start with a fairly small value (so the initial iteration will resemble Gauss–Newton), then at each iteration:

- If, as a result of the step suggested by Eq. (37), the cost function increases, do not update the state vector and increase γ.
- If the cost function is decreased by a step, update the state vector and decrease γ for the next step.

ORAC uses a factor of 10 for increasing and reducing γ. The scaling matrix, $\mathbf{D}_n$, is used to ensure that the state parameters are of similar magnitude, in the interests of numerical stability.

This iterative procedure is continued until either a convergence criterion is satisfied, or a maximum number of iterations is exceeded (in the former case the retrieval is said to have converged, while the later case can generally be rejected as a failed retrieval). ORAC uses the change in the cost function between iterations to determine whether the algorithm has converged – a negligible change in cost between iterations indicates that the retrieval is no longer improving the fit between measurements and forward model.

The optimal estimation framework offers two main advantages over more ad hoc retrieval algorithms:

1. *A priori* information is explicitly included in the retrieval in a way which is consistent with the way measurement information is included.
2. Rigorous error propagation, including the incorporation of forward model and forward model parameter error, is built into the system, providing extra quality control and error estimates on the retrieved state.

Error estimates for the retrieved state can be calculated by applying

$$\hat{\mathbf{S}} = \mathbf{S}_{\mathrm{a}}^{-1} + \mathbf{K}_i^T \mathbf{S}_{\varepsilon}^{-1} \mathbf{K}_i \tag{39}$$

after the final iteration, where $\hat{\mathbf{S}}$ is the covariance of the retrieved state. If there is a known limitation in the forward model, due to approximations or incomplete modeling of the relevant physics, this can be accounted for in the retrieval as forward model error described by a covariance matrix $\mathbf{S}_{\mathrm{fm}}$. Uncertainty in parameters on which the forward model depends, but which are not retrieved (for instance, the height distribution of aerosol), can also be included in the retrieval as forward model parameter error. These extra error terms are combined with the measurement error:

$$\mathbf{S}_{\mathrm{y}} = \mathbf{S}_{\varepsilon} + \mathbf{S}_{\mathrm{fm}} + \mathbf{K}_{\mathrm{p}} \mathbf{S}_{\mathrm{p}} \mathbf{K}_{\mathrm{p}}^T, \tag{40}$$

where $\mathbf{S}_{\mathrm{p}}$ is the covariance matrix describing the uncertainty in the forward model parameters and $\mathbf{K}_{\mathrm{p}}$ is the weighting function which maps this error into measurement space (i.e. it is analogous to the $\mathbf{K}_i$ matrix used above). The new measurement covariance $\mathbf{S}_{\mathrm{y}}$ then replaces $\mathbf{S}_{\varepsilon}$ in Eq. (36) to (39).

9. Aerosol speciation

Although the ORAC algorithm does not directly retrieve any information on the composition of the aerosol, except the change in mixing state implied by the retrieval of effective radius (see Section 3.1), it is still possible for the system to provide some indication of the aerosol type present in a given scene. This capability is achieved by running the retrieval

repeatedly using a different predefined aerosol class each time. The resulting set of aerosol retrievals can be merged into a single 'speciated' product by comparing the retrieval cost function for each of the aerosol classes used, weighted by *a priori* knowledge of the likely aerosol type at that particular location.

For example, over the mid-Atlantic Ocean, the dominant aerosol would be expected to be maritime. However, during periods of agricultural and forest burning in central and southern Africa, a biomass aerosol class will often provide a significantly better fit to the measurements (as indicated by a lower value of the cost function), indicating the presence of outflow from the African fires.

Although this method has been found to be somewhat successful, it is subjective in nature (relying on an ad hoc *a priori* weighting of the cost function comparison) and can only be considered as an indicative measure of the actual aerosol composition. Also, the method is only sensitive to aerosol types which appear significantly different in the measurement channels. For instance, it has been found that when using (A)ATSR or SEVIRI visible channels, maritime aerosol and desert dust are difficult to distinguish except at very high optical depths.

10. Example results

The following sections give examples of aerosol properties derived using the different versions of ORAC described in the previous sections.

10.1 Single-view retrieval from AATSR

Fig. 7.3 shows monthly means of optical depth, effective radius and speciation for September 2004, from AATSR, as retrieved using the Lambertian Fast-FM described in Section 5. Nadir view AATSR radiances have been cloud cleared and then averaged onto a 10 km sinusoidal grid [33] prior to retrieval. Cloud clearing over the ocean used the ESA operational cloud flag [10], while over the land a custom method, which uses a threshold on normalized difference vegetation index values derived from the 0.55, 0.67 and 0.87 μm channels, as well as thresholds on the radiances in these channels themselves [2] was used. The retrieval has been run using five separate aerosol classes:

- continental clean †
- desert dust †
- maritime clean †
- urban †
- biomass burning ‡

where a † indicates the aerosol class originates from the OPAC database [11] and ‡ originates from the work of Dubovik et al. [9]. The monthly mean was performed on a $1^{\circ} \times 1^{\circ}$ latitude/longitude grid and the data has had the following quality-control criteria applied:

- The retrieval must have converged.
- The final value of the retrieval cost function must be below a threshold value.
- The retrieval must have converged to a state within the bounds of the LUTs.
- The retrieved surface reflectance at 550 nm must be less than 0.2.

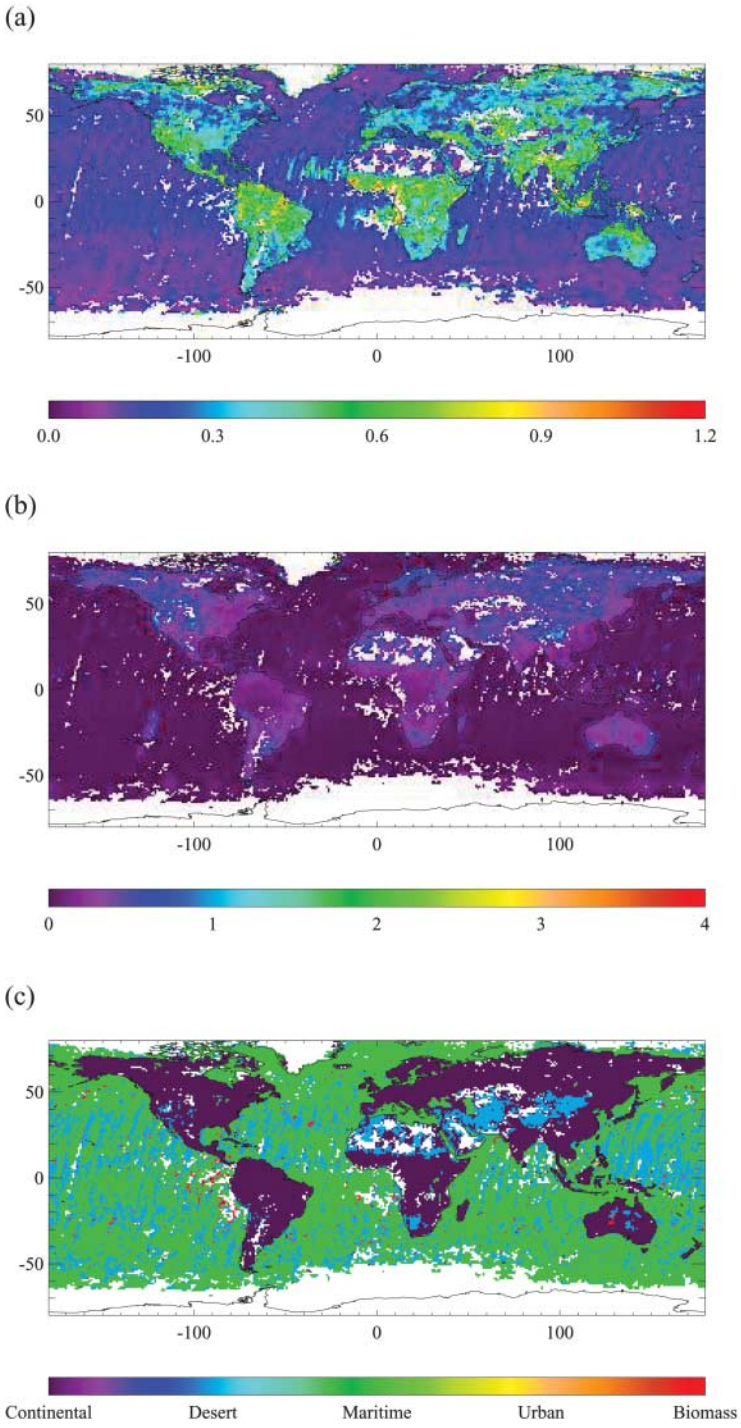

Fig. 7.3. Global mean (a) 0.55 μm aerosol optical depth, (b) effective radius in μm and (c) speciation from AATSR for the month of September 2004.

- Over land pixels the fraction of measurement pixels within a given sinusoidal grid cell flagged as cloud must be less than 50 %.[6]

The first thing to note from Fig. 7.3 is the limitations introduced by the narrow swath of AATSR. Since ORAC uses the visible wavelength channels of AATSR, only data from the descending (daylight) half of the orbit can be used. Even with a month of data, there remain areas where cloud cover and sunglint mean there is no coverage, and the retrieved fields still show evidence of the orbital pattern. Taking this into account, the optical depth field shows the expected patterns, with reasonable values. However, the limitations of the single view using a Lambertian surface reflectance are clear, especially over land. Generally, retrievals over land surfaces show slightly higher than expected optical depths and there is a clear step change in both optical depth and effective radius along coastal boundaries. It is also notable that some regions which would be expected to show high aerosol loading, such as China, are not particularly conspicuous in the optical depth field. The optical depth over the oceans appears to be much more as expected, although a very low value of effective radius has been retrieved. Speciation (Fig. 7.3(c)) shows that the expected aerosol class is derived for most pixels, although there is clear evidence of the difficulty in distinguishing desert dust and maritime aerosol using the AATSR channels. Also, there is little indication of the biomass burning plume visible in the optical depth field off the coast of Africa.

These conclusions are supported by Fig. 7.4, which displays the results a comparison between AERONET optical depths and AATSR retrievals for the same month as in Fig. 7.3. Fig. 7.5 shows the locations of the AERONET stations used in the comparisons presented in this chapter. The stations used have been limited to those known to provide measurements which are representative of their surrounding area, based on recommendations by S. Kinne [16]. These comparisons relate the mean AERONET optical depth within 30 minutes of the satellite overpass with the mean satellite optical depth within 20 km of the AERONET site. This averaging is done to try and ensure that similar airmasses are being measured by the satellite and ground-based instruments and is based on the procedure used for MODIS aerosol validation [12]. Each AERONET station used in the comparison has been assigned a unique coloured symbol, with stations within similar geographical regions having the same color. Stations which are in open sea or coastal sites are denoted with open symbols, while solid symbols are used for inland sites. The ORAC data used for comparison with AERONET have had the same filters applied as those applied for the monthly mean products, with the addition of a threshold of the variability of the retrieved optical depth within the 20 km spatial window, which was included to remove cases where high spatial variablity in aerosol loading could introduce significant sampling biases to the comparison.

The comparison with AERONET data clearly shows that the retrieval is performing relatively poorly over land surfaces. The high optical depth bias of the single-view Lambertian ORAC results suggested by the monthly mean plot is confirmed, and the results show a great deal of scatter, with a correlation of 0.4 between the two datasets. The results

[6] The scheme averages all pixels cloud-free within each sinusoidal grid cell, to give a cloud free radiance. However, the cloud flag applied to AATSR over the land was found to leave some residual cloud contamination. This was not found to be a problem over ocean pixels.

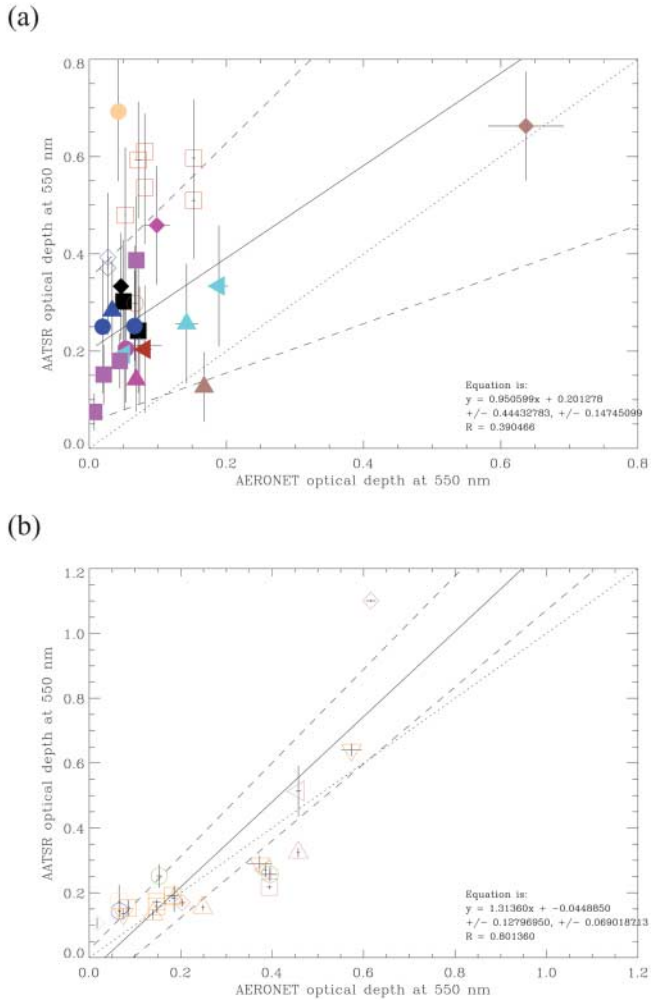

Fig. 7.4. Scatterplots of AERONET optical depth at 550 nm versus coincident AATSR retrievals for September 2004 from the single-view Lambertian surface retrieval. The results are a composite of five separate aerosol classes, with the class of each point being determined by comparing the retrieval costs. Error bars indicate the standard deviation of the values that went into the spatial or temporal averaging. Each plot includes a least-absolute-deviation fit line (solid line) and its equation, plus uncertainty estimates on this fit (dashed lines), with the uncertainties in the fitted parameters included below the equation. The one-to-one line (dotted) is also included for comparison, and the correlation coefficient for the plot, R is given. Plot (a) shows results for inland AERONET stations. Plot (b) shows results for coastal stations, where only satellite results over the ocean are compared.

for ocean pixels are far more encouraging. Here there is no clear bias in the results and there is much less scatter, with the correlation being 0.8.

These results show that the single-view Lambertian retrieval is very dependent on an accurate *a priori* description of the surface reflectance. The higher reflectance and much greater anisotropicity (and hence greater uncertainty in its reflectance) of the land surface, when compared to the ocean, results in relatively poor retrieval performance over the land.

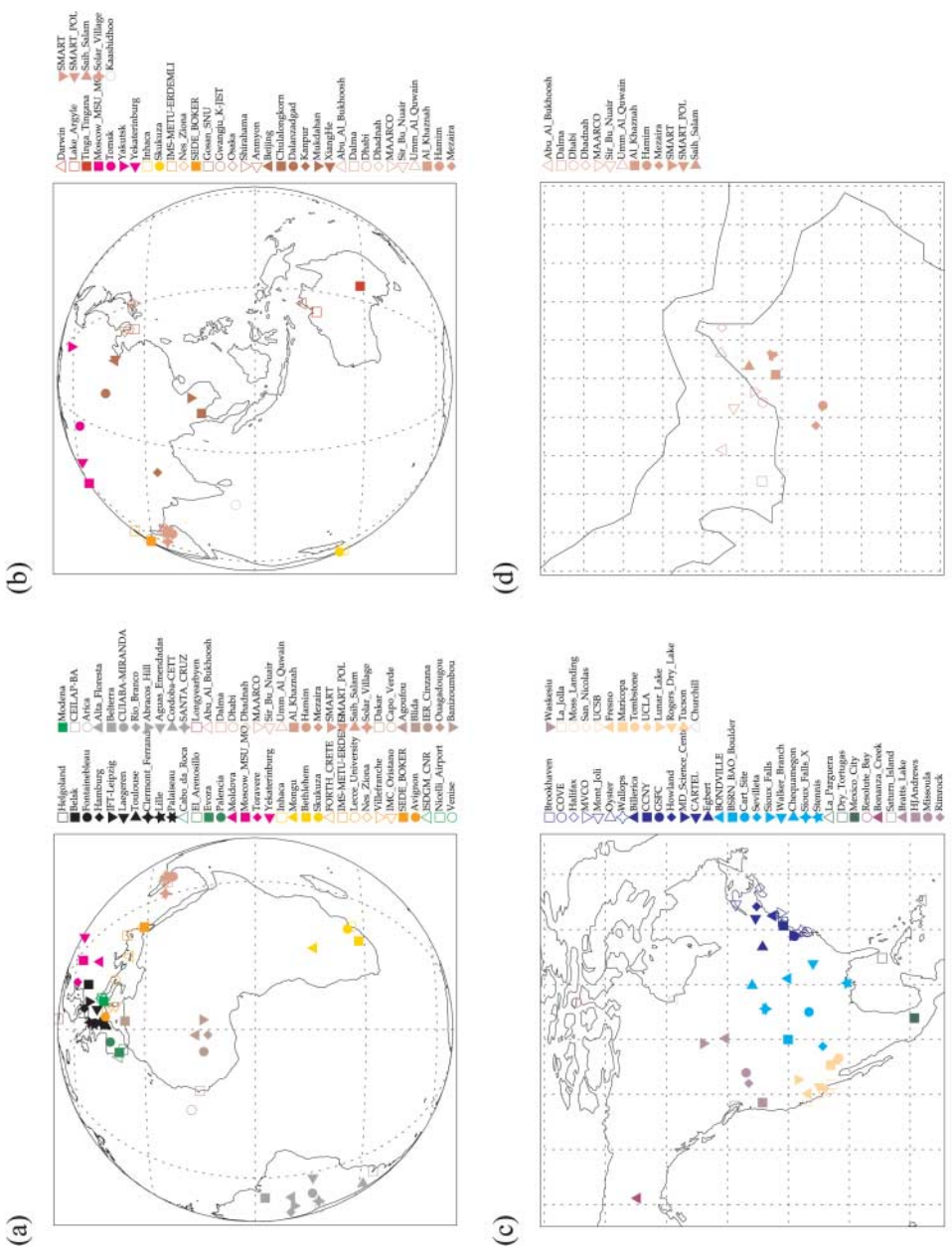

Fig. 7.5. AERONET stations used in the comparisons discussed in this chapter. (a) shows those stations within the SEVIRI observation disk, (b) shows stations within the Eastern Hemisphere, North American stations appear in (c) and those in Arabia are shown in (d).

10.2 Dual-view retrieval from AATSR

This section presents results equivalent to those presented in Section 10.1, but using the BRDF surface reflectance version of ORAC incorporating both views of the AATSR instrument. Fig. 7.6 can be exactly compared to Fig. 7.3 and shows a marked improvement in the retrieved aerosol properties. The optical depth field shows far less evidence of elevated optical depths over land pixels and is much more continuous across coastal boundaries. Areas of high optical depth are evident, but are generally in regions where high aerosol loading is to be expected – such as Southern and Eastern Asia). Optical depths in desert regions are also more believable than in the single-view Lambertian results. The effective radius field shows features that are also expected such as larger particles in regions of desert outflow, and smaller particles associated with polluted regions. Speciation also shows evidence of improvement over the single-view Lambertian results, with significant amounts of biomass-burning aerosol being detected in regions where it might be expected (the Amazon Basin and central/southern Africa) as well as clear biomass plume extending across the Alantic (which even shows evidence of aging – becoming more like background continental aerosol as it extends towards South America). However, there is still evidence of the difficulty in distinguishing desert dust and maritime aerosol over the sea and at high latitudes the speciation over the sea breaks down somewhat (with a scattering of different aerosol types being retrieved). The reason for this is not clear; however it could due to the phase functions of the various aerosol types producing similar spectral responces across the AATSR channels at high solar zenith angles.

Comparison with AERONET data (Fig. 7.7) offers further evidence of the improved quality of these results with those discussed in Section 10.1. In this instance all of the comparisons (land and sea) have been plotted together and show a very high degree of correlation (over 0.95) and very little bias. This level of correlation is extremely impressive, given the widely different methods and sampling used to make the measurements.

Comparing the results from this section and Section 10.1 shows the great improvement given by the BRDF surface reflectance Fast-FM. This improvement is due to three factors:

1. The surface reflectance is better modeled. This is particularly important for anisotropic land surfaces and in regions of the ocean effected by sunglint, where the Lambertian approximation breaks down.
2. The retrieval is able to make use of the AATSR dual-view measurement system. Not only does this double the number of measurements available to the retrieval but, since each surface pixel is viewed twice through differing atmospheric paths, the constraint on both the surface reflectance and aerosol properties being consistent between views allows the retrieval to decouple their effects much more effectively than with a single view.
3. The inclusion of four more measurements provides enough information for the retrieval of the surface reflectance in each channel independently, greatly reducing the reliance on an accurate *a priori* knowledge of it.

Although it is difficult to disentangle these three effects, the results do strikingly demonstrate the strength of the ATSR dual-view system.

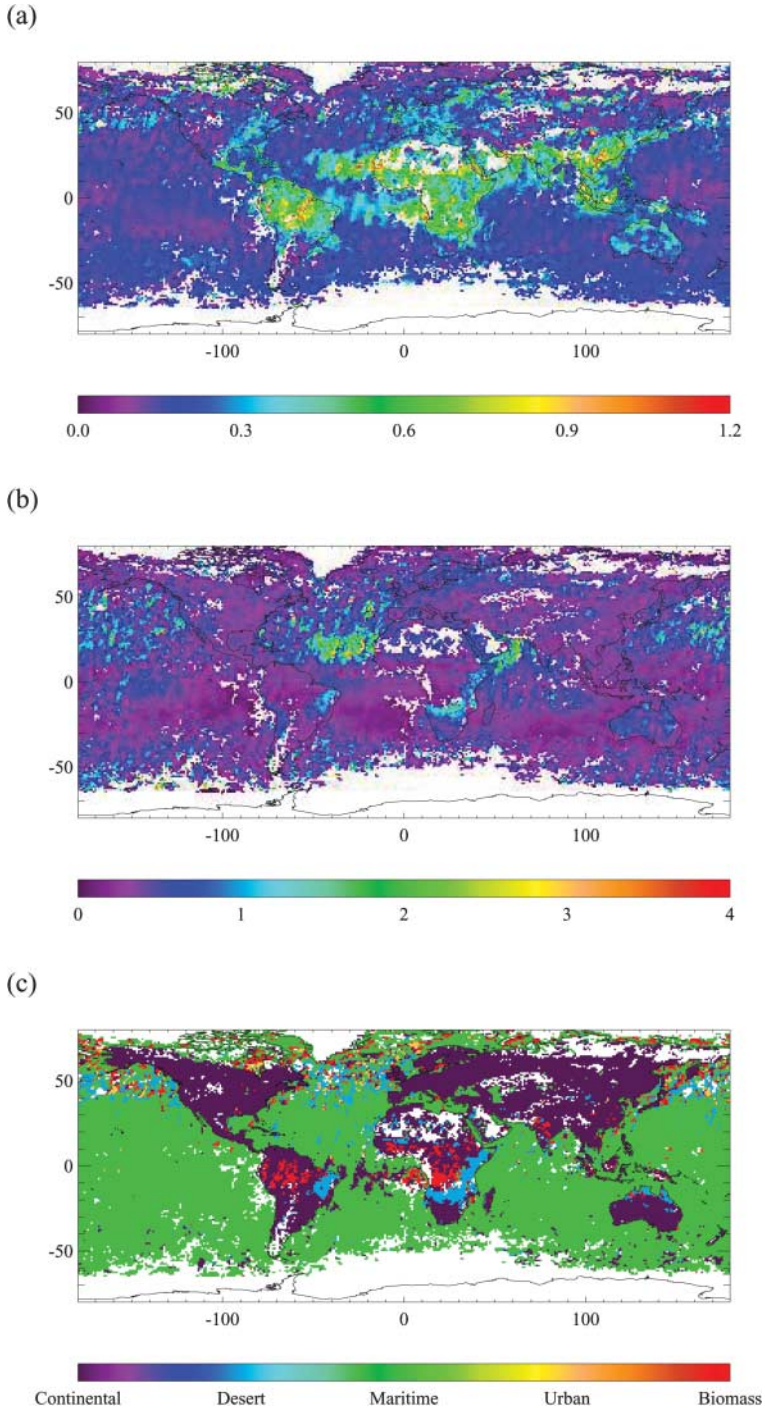

Fig. 7.6. Global mean (a) 0.55 μm aerosol optical depth, (b) effective radius and (c) speciation from AATSR for the month of September 2004. The data were produced by the BRDF version of ORAC, using both nadir and forward views on a $\sim$ 10 km sinusoidal grid. The monthly mean was performed on a $1^\circ \times 1^\circ$ latitude/longitude grid.

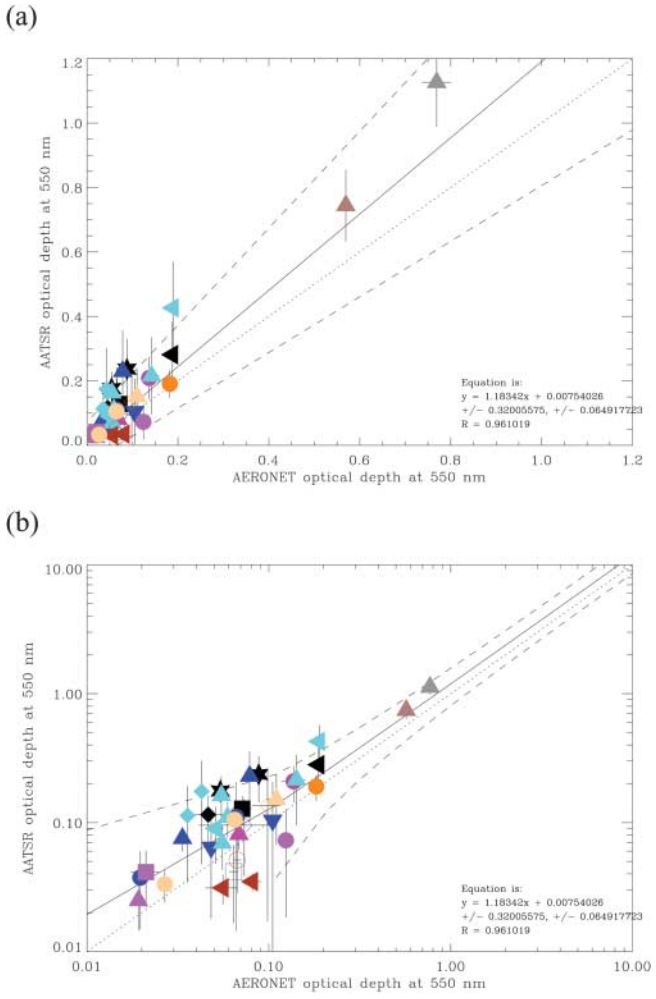

Fig. 7.7. Scatterplots of AERONET optical depth at 550 nm versus coincident AATSR retrievals for September 2004 from the dual-view BRDF retrieval. The results are a composite of five separate aerosol classes, with the class of each point being determined by comparing the retrieval costs. Both plots show the results for all AERONET stations, with (b) using a logarithmic scale for clarity. See Fig. 7.5 for a definition of the plotting symbols.

10.3 Retrieval from SEVIRI using the BRDF Fast-FM

Fig. 7.8 shows the mean 0.55 μm optical depth retrieved from SEVIRI data over September 2004, as given by ORAC using the BRDF forward model. The production of this composite followed a very similar method as used for the AATSR monthly means discussed in the previous two sections. The same retrieval grid and aerosol classes were used, and very similar quality controls were applied. The composite has been formed using two SEVIRI measurements per day, one at 10:15 and one at 16:15 UT. Although SEVIRI does not

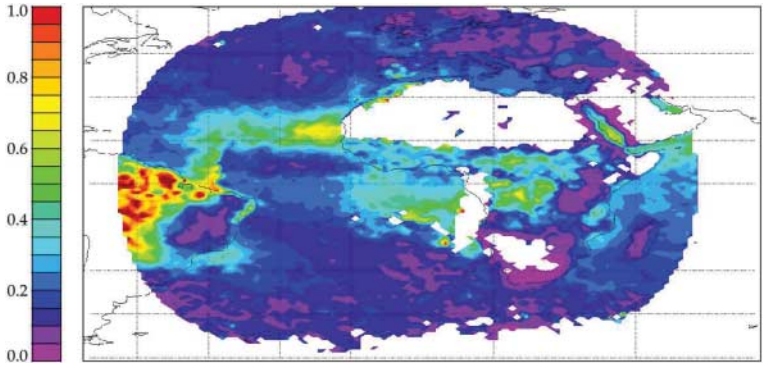

Fig. 7.8. Global mean 0.55 μm aerosol optical depth from SEVIRI for the month of September 2004. The data were produced by the BRDF version of ORAC, on a $\sim$ 10 km sinusoidal grid. The monthly mean was performed on a $1^\circ \times 1^\circ$ latitude/longitude grid. Speciation has been carried out in the usual way, from the same set of five aerosol classes used for the AATSR retrievals.

provide a dual-view measurement, the BRDF forward model still provides a better description of the surface reflectance than the Lambertian approximation does. One of the largest difficulties to be overcome when applying the ORAC scheme to SEVIRI data is that of cloud-contamination. This is largely due to the larger pixel size of the SEVIRI instrument when compared to the (A)ATSR sensors, which results in relatively large number of cloud contaminated pixels being flagged as clear by the operational EUMETSAT SEVIRI cloud flag. Although post-retrieval quality control has removed the vast majority of residual cloud contamination, there is still some evidence of contaminaton in the very high average optical depths seen in the Amazon basin.

Fig. 7.9 shows that, as far as agreement with AERONET is concerned, the SEVIRI retrieval lies somewhere between the AATSR single-view Lambertian and dual-view BRDF results. Agreement over the ocean is excellent, with a correlation of 0.79 and very little bias. For land-based stations, the best-fit line shows a strong negative bias. However, it can be seen that this is mostly caused by a bias against a single AERONET station – Mongu (denoted by yellow triangles). This station lies in an arid region of southern Africa (see Fig. 7.5(a)) that is characterized by a high surface reflectance. This suggests that the SEVIRI retrieval is prone to underestimating aerosol optical depth in regions where the surface component dominates the TOA signal. The negative bias in the SEVIRI results apparent when compared against another desert AERONET site, Blida (denoted by brown squares), supports this conclusion. Furthermore, if Fig. 7.8 is compared to Fig. 7.6, it can be seen that the SEVIRI-based optical depth does tend to be lower than the AATSR value in arid regions. Although the SEVIRI results have had a stringent surface reflectance threshold applied to them (resulting in the regions of missing data over the Sahara, Arabia and southern Africa), these results suggest that a stronger quality-control criterion may be needed.

If one neglects the Mongu points in Fig. 7.9, the agreement between SEVIRI and AERONET is again excellent. Indeed, even with the Mongu points included in the calculation, the correlation for inland AERONET stations is actually higher than that for the ocean/coastal sites, at 0.82. This high correlation is largely due to excellent agreement

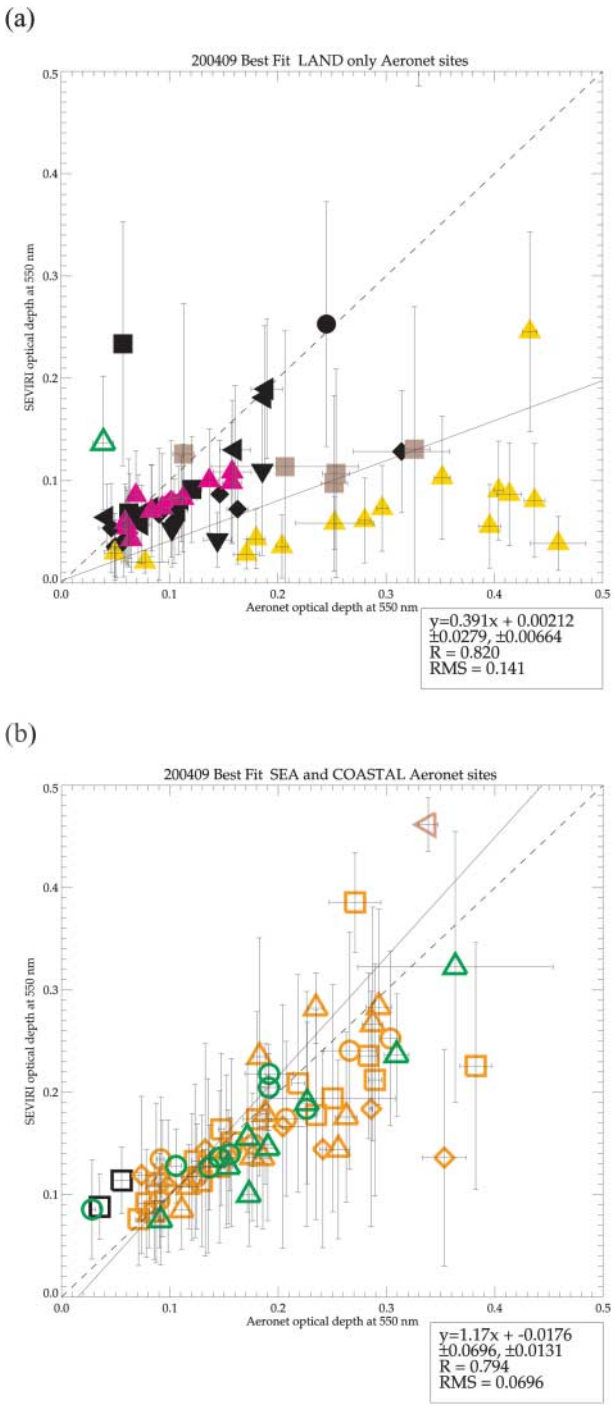

Fig. 7.9. Scatter-plots of AERONET optical depth at 550 nm versus coincident SEVIRI retrievals for September 2004. Plot (a) shows results for inland AERONET stations. Plot (b) shows results for coastal stations, where only satellite results over the ocean are compared. See Fig. 7.5 for a definition of the plotting symbols.

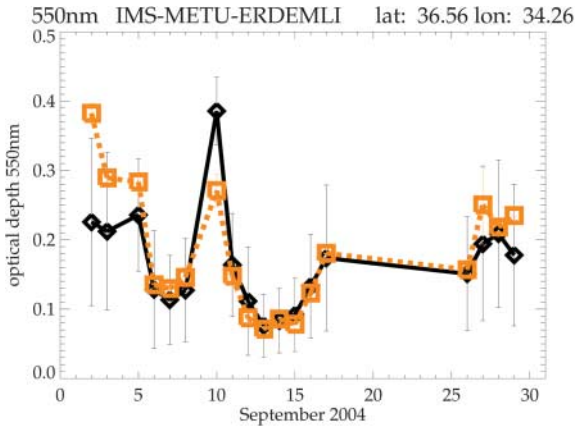

Fig. 7.10. A time-series of 0.55 μm optical depth from SEVIRI retrievals (black) and AERONET sun-photometer (orange). Only retrievals over land pixels were considered in computing the SEVIRI optical depth.

between the ORAC retrieval and AERONET over Europe. An example of this is shown in Fig. 7.10, where time series of collocated AEROSOL optical depth from SEVIRI and the IMS-METU-ERBEMLI AERONET station are given. In almost all cases the two measurements agree within the error bars.

10.4 Retrieval using the thermal infrared forward model

At the time of writing, work on including a thermal infrared forward model in the ORAC aerosol retrieval was still at a fairly early stage. However, the retrieval has been applied to a limited quantity of SEVIRI data from March 2006. This month was marked by a very large dust storm in the Sahara, which resulted in large plumes of dust being blown south, towards the Ivory Coast. There the lofted dust encountered a strong westerly airflow, which carried it out into the Atlantic at extremely high concentrations. Fig. 7.11 shows the SEVIRI data collected on March 9, 2006, at the height of the event. The false color image clearly shows the dust plume extending in a northwesterly direction across the Atlantic, but also demonstrates the problem encountered when trying to retrieve lofted dust over a desert surface using a visible/near-infrared retrieval scheme – it is very difficult to distinguish the lofted dust from the background surface over the desert in Fig. 7.11(a).

Fig. 7.11(b) shows the 550 nm optical depth retrieved using ORAC with the thermal forward model enabled. In this instance the aerosol class has been assumed to be desert dust (based on the optical properties of Peters et al. [24]), and the maximum optical depth covered by the LUTs has been extended from 2 to 5. The retrieval has been performed on a 10-km sinusoidal grid. The dust plume extending into the Atlantic is very clear, and shows extremely high optical depths, which in some places exceed 5. The optical depth field also shows the plume extending along the southern edge of the Sahara, and shows elevated optical depths (exceeding 1) extending north into the Sahara itself.

It must be noted that Fig. 7.11 also shows evidence of the need for further development of the thermal-infrared retrieval. The differentiation of heavy dust loading and cloud is a

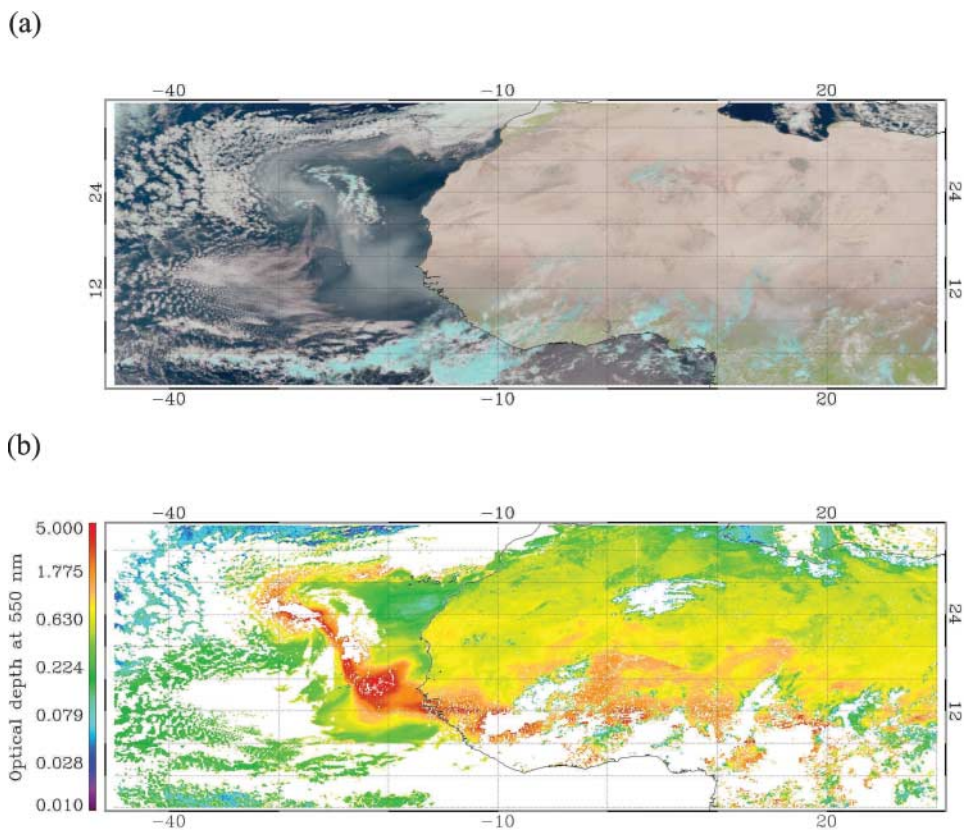

Fig. 7.11. An example of retrieved optical depth making use of thermal channels. Plot (a) shows a false-color image from SEVIRI taken on March 9, 2006, at approximately 12:12UT, during a large dust storm event in the southern Sahara. Plot (b) shows the retrieved optical depth field for this scene. White areas in plot (b) indicate the presence of cloud or failed retrievals (due, for example, to the optical depth being outside the 0.01 to 5.0 optical depth range).

difficulty common among aerosol retrieval schemes, and it is a problem with the thermal-infrared version of ORAC as well. The optical depth field also shows features which are in reality clearly associated with the surface. This is due to both limitations in the description of the surface and the applicability of the assumed aerosol properties. Steps are being taken to address these issues, namely:

- The description of the surface reflectance in the thermal-infrared retrieval will be improved by incorporating the visible/near-infrared BRDF Fast-FM.
- The use of non-spherical scattering code in the calculation of LUTs for non-spherical aerosol classes (such as desert dust) is being investigated.
- Further measurements of Saharan aerosol samples will be undertaken.
- It is hoped that a surface BRDF product derived from SEVIRI measurements will become available in the future [35], which will provide an improved description of the surface for the retrieval.

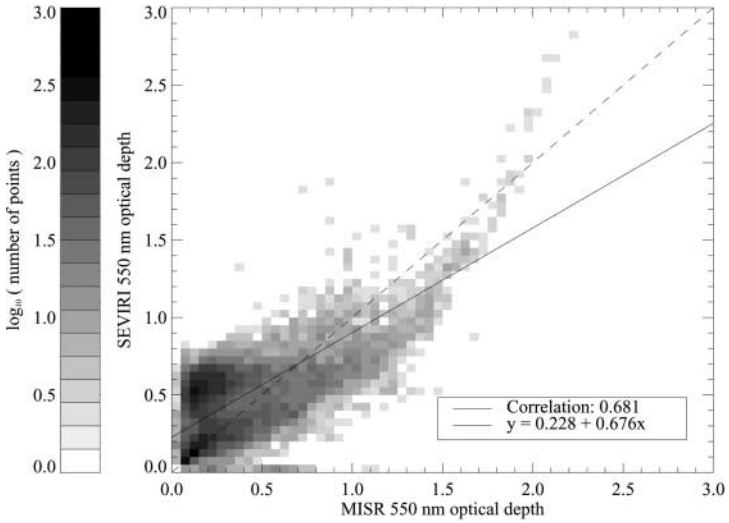

Fig. 7.12. Scatter between collocated SEVIRI and MISR optical depths over the Saharan region for the period March 5–30, 2006. The SEVIRI results, all of which are for 12:12UT, have been retrieved with the thermal-infrared version of ORAC on a 10 km sinusoidal grid, which has then been interpolated onto the MISR level 2 optical depth grid. The 1-to-1 line is indicated by the dashed line, while the solid line gives the best-fit line (least absolute deviation fit, weighted by the error in both datasets), the equation of which is also given.

Despite these limitations, however, these results do provide a good overall indication of aerosol optical depth field. Fig. 7.12 shows a comparison between collocated thermal-infrared ORAC and MISR (Multi-angle Imaging SpectroRadiometer) retrievals. Due to its multiple-view observation system, MISR is regarded as one of the most reliable satellite-based aerosol products, particularly over bright surfaces like deserts [8]. The agreement between the two datasets is very close, especially considering the difference in measurement time between the two (MISR observes at approximately 11:30 local solar time, which means only MISR swaths which lie near the east coast of the Saharan region will be temporally close to the SEVIRI measurement).

11. Conclusion

This chapter has detailed the ORAC aerosol retrieval algorithm in its various forms. ORAC is a retrieval scheme based around the optimal estimation framework [26, 27] that uses a plane parallel radiative transfer, using assumed aerosol properties, to forward model the TOA radiance measured by satellites. The basic ORAC algorithm provides a framework for the retrieval of aerosol properties from visible/infrared radiometers. As demonstrated by the variety of different ORAC variants described, the generic nature of the algorithm makes it suitable for a wide range of instruments, provided they meet the following criteria:

- The measured signal is not polarization-dependent.
- The measured signal is not strongly effected by molecular Rayleigh scattering, as the variation of this signal with topography height and atmospheric state is not modeled.

- The channels used in the retrieval are fairly free of molecular absorption by atmospheric trace gases.
- Instrument and solar zenith angles must be less than $\sim 80^\circ$ for the plane parallel radiative transfer used in the forward model to be reliable.

The algorithm can also be easily modified to make use of different forward models, a feature which has allowed the development of the BRDF, ATSR dual-view and thermal-infrared versions of the algorithms presented.

The example results presented demonstrate that the ORAC algorithm shows good agreement with ground-based measurements of aerosol optical depth, as well as with current operational satellite aerosol products. The quality of the products combined with the adaptability of the algorithm, makes the ORAC algorithm unique in its ability to quickly adapt to a range of different instruments. This, combined with the strengths inherent in an optimal estimation retrieval scheme, namely:

- statistically rigorous error propagation and error estimates on all retrieved quantities,
- the inclusion of *a priori* information in a statistically consistent way,

make ORAC a strong addition to the stable of satellite aerosol retrieval algorithms.

References

1. A. Berk, L.S. Bernstein, G.P. Anderson, P.K. Acharya, D.C. Robertson, J.H. Chetwynd, and S.M. Adler-Golden. MODTRAN cloud and multiple scattering upgrades with application to AVIRIS. *Remote Sens. Environ.*, **65**:367–375, 1998.
2. A. Birks. Improvements to the AATSR IPF relating to land surface temperature. technical note, European Space Agency, 2004.
3. E. Carboni, G.E. Thomas, R.G. Grainger, C.A. Poulsen, R. Siddans, D. Peters, E. Campmany, A. M. Sayer, H.E. Brindley. Retrieval of aerosol properties from SEVIRI using visible and infrared channels. *Proceedings of EUMETSAT/AMS Conference*, Amsterdam, 24–28, 2007.
4. C.S. Cox, W.H. Munk. Measurement of the roughness of the sea surface from photographs of the Sun's glitter. *J. Opt. Soc. Am.*, **44**:838–850, 1954.
5. C.S. Cox, W.H. Munk. Statistics of the sea surface derived from Sun glitter. *J. Mar. Res.*, **13**:198–227, 1954.
6. G.A. dÁlmeida, P. Koepke, E.P. Shettle. *Atmospheric Aerosols: Global Climatology and Radiative Characteristics*. A Deepak Publishing, Hampton, Virginia, 1991.
7. C.N. Davies. Size distribution of atmospheric particles. *J. Aerosol Sci.*, **5**:293–300, 1974.
8. D.J. Diner, L. Di Girolamo, A. Nolin. Preface to the MISR Special Issue. *Remote Sens. Environ.*, **107**:1–2, 2007.
9. O. Dubovik, B. Holben, T.F. Eck, A. Smirnov, Y.J. Kaufman, M.D. King, D. Tanre, I. Slutsker. Variability of absorption and optical properties of key aerosol types observed in worldwide locations. *J. Atmos. Sci.*, **59**:590–608, 2002.
10. European Space Agency. *ESA AATSR Product Handbook*, Issue 2.2, 2007.
11. M.P. Hess, P. Koepke, I. Schult. Optical properties of aerosols and clouds: the software package OPAC. *Bull. Am. Met. Soc.*, **79**:831–844, 1998.
12. C Ichoku, D.A Chu, S. Mattoo, Y.J. Kaufman, L.A. Remer, D. Tanre, I. Slutsker, B.N. Holben. A spatio-temporal approach for global validation and analysis of MODIS aerosol products. *Geophys. Res. Lett.*, **29**(12.1616), 2002.
13. Y. Jin, C.B. Schaaf, C.E. Woodcock, F. Gao, X. Li, A.H. Strahler. Consistencey of MODIS surface BRDF/albedo retrievals: 2. Validation. *J. Geophys. Res.*, **108**(D5), 2003. doi:10.1029/2002JD002804.
14. Y. Jin, C.B. Schaaf, C.E. Woodcock, F. Gao, X. Li, A.H. Strahler, W. Lucht, S. Liang. Consistency of MODIS surface BRDF/albedo retrievals: 1. Algorithm performance. *J. Geophys. Res.*, **108**(D5), 2003. doi:10.1029/2002JD002803.

15. C.G. Justus, M.V. Paris. Modelling solar spectral irradiance and radiance at the bottom and top of a cloudless atmosphere. *J. Appl. Meteorol.*, **24**:193–205, 1985.
16. S. Kinne. Private communication, 2007.
17. P. Koepke. Effective reflectance of oceanic whitecaps. *Appl. Opt.*, **23**:1816–1824, 1984.
18. J.-F. Léon, D. Tanré, J. Pelon, Y.J. Kaufman, J.M. Haywood, B. Chatenet. Profiling of a Saharan dust outbreak based on a synergy between active and passive remote sensing. *J. Geophys. Res.*, **108**(D18), 2003. doi:10.1029/2002JD002774.
19. C.J. Merchant, O. Embury, P. Le Borgne, B. Bellec. Saharan dust in nighttime thermal imagery: detection and reduction of related biases in retrieved sea surface temperature. *Remote Sensing Env.*, **104**:15–30, 2006.
20. G. Mie. Beiträge zur Optik trüber Medien, speziell kolloidaler Metallösungen. *Ann. Phys.*, **25**:377–445, 1908.
21. E.C. Monahan, I. Ó Muircheartaigh. Optimal power-law description of oceanic whitecap coverage dependence on wind speed. *J. Phys. Oceanogr.*, **10**:2094–2099, 1980.
22. André Morel, Louis Prieur. Analysis of variations in ocean color. *Limnol. Oceanogr.*, **22**:709–722, 1977.
23. J.M. Nicolas, P.Y. Deschamps, R. Frouin. Spectral reflectance of oceanic whitecaps in the visible and infra-red: aircraft measurements over open ocean. *Geophys. Res. Lett.*, **28**:4445–4448, 2001.
24. D.M. Peters, R.G. Grainger, G.E. Thomas, R.A. McPheat. Laboratory measurments of the complex refractive index of Saharan dust aerosol. *Geophys. Res. Abstracts*, **9**, 2007.
25. P.J. Rayer. Fast transmittance model for satellite sounding. *Appl. Opt.*, **34**:7387–7394, 1995.
26. C.D. Rodgers. Retrieval of atmospheric temperature and composition from remote measurements of thermal radiation. *Rev. Geophys. and Space Phys.*, **14**:609–624, 1976.
27. C.D. Rodgers. *Inverse Methods for Atmospheric Sounding: Theory and Practice.* World Scientific, 2000.
28. J.G. Salomon, C.B. Schaaf, A.H. Strahler, F. Gao, Y. Jin. Validation of the MODIS bidirectional reflectance distribution function and albedo retrievals using combined observations from the AQUA and TERRA platforms. *IEEE Trans. Geosci. Remote Sens. Environ.*, **83**(6):1555–1565, 2006.
29. R.W. Saunders. RTTOV-7 science and validation report. RTTOV documentation, NWP SAF, 2002. http://www.metoffice.com/research/interproj/nwpsaf/rtm.
30. A. M. Sayer. A sea surface albedo model suitable for use with AATSR aerosol retrieval, version 2. Technical memorandum, Atmospheric, Oceanic and Planetary Physics, University of Oxford, 2007. http://www.atm.ox.ac.uk/main/research/technical/2007.2.pdf.
31. F.M. Schulz, K. Stamnes, F. Weng. Vdisort: An improved and generalized discrete ordinate method for polarized (vector) radiative transfer. *J. Quant. Spectrosc. Radiat. Transfer*, **61**(1):105–122, 1999.
32. C.L. Shaaf. *MODIS BRDF/Albedo Product (MOD43B) User's Guide.* Boston University, 2004. http://www-modis.bu.edu/brdf/userguide/index.html.
33. J.P. Snyder. Map projections – a working manual. Professional Paper 1395, U.S. Geological Survey, 1987.
34. K. Stamnes, S.C. Tsay, W. Wiscombe, K. Jayaweera. A numerically stable algorithm for discrete-ordinate-method radiative transfer in multiple scattering and emitting layered media. *Appl. Opt.*, **27**:2502–2509, 1988.
35. S. Wagner, Y. Govaerts, A. Lattanzio, P. Watts. Simultaneous retrieval of aerosol load and surface reflectance using MSG/SEVIRI observations. *Geophys. Res. Abstracts*, **9**, 2007.
36. W. Wanner, A.H. Strahler, P. Lewis B. Hu, J.-P. Muller, X. Li, C.L. Barker Schaaf, M.J. Barnsley. Global retrieval of bidirectional reflectance and albedo over land from EOS MODIS and MISR data: theory and algorithm. *J. Geophys. Res.*, **102**(D14):17,143–17,161, 1997.
37. P.D. Watts, C.T. Mutlow, A.J. Baran, A.M. Zavody. Study on cloud properties derived from Meteosat Second Generation observations. ITT 97/181, EUMETSAT, 1998.